

Active mechanical haptics with high-fidelity perceptions for immersive virtual reality

Received: 20 November 2022

Accepted: 5 May 2023

Published online: 29 May 2023

 Check for updates

Zhuang Zhang^{1,2,7}, Zhenghao Xu^{3,7}, Luoqian Emu¹, Pingdong Wei^{1,2},
Sentao Chen¹, Zirui Zhai⁴, Lingyu Kong⁵, Yong Wang³ &
Hanqing Jiang^{1,6,2}  

Human-centred mechanical sensory perceptions enable us to immerse ourselves in the physical environment by actively touching or holding objects so that we may feel their existence (that is, ownership) and their fundamental properties (for example, stiffness or hardness). In a virtual environment, the replication of these active perceptions can create authentic haptic experiences, serving as an essential supplement for visual and auditory experiences. We present here a first-person, human-triggered haptic device enabled by curved origami that allows humans to actively experience touching of objects with various stiffness perceptions from soft to hard and from positive to negative ranges. This device represents a substantial shift away from the third-person, machine-triggered and passive haptics currently in use. The device is synchronized with the virtual environment by changing its configuration to adapt various interactions by emulating body-centred physical perceptions, including hardness, softness and sensations of crushing and weightlessness. Quantitative evaluations demonstrate that the active haptic device creates a highly immersive virtual environment, outperforming existing vibration-based passive devices. These concepts and resulting technologies create new opportunities and application potential for a more authentic virtual world.

The emerging metaverse powered by virtual reality (VR) and augmented reality (AR) technologies is transforming present digital media viewed in the third person to a future immersive platform that vividly represents the physical environment perceived in the first person^{1–3}. This is achieved by constructing a virtual environment with authentic sensory perceptions, including but not limited to sight, hearing and touch. In this new paradigm of how humans engage with future media, VR/AR technologies are primed to permeate a range of industry sectors (for example, entertainment, communications, education, human–machine interaction, teleoperation, clinical therapy and rehabilitation), while aided by advanced software (that is, communication technologies, various apps and social networks) and hardware (that is, VR/AR and

haptic devices) to enhance our VR/AR haptic experiences^{4,5}. Although state-of-the-art VR/AR devices offer stereoscopic visual and auditory sensory perceptions, they fail in delivering a concrete sensory dimension in the mechanical domain, namely, touch sensation^{5–7}. Substantial progress has been made to make the virtual world touchable by bringing machine-triggered, passive haptic experiences to users. However, most induce simple hand-centred^{5–16} or cutaneous^{17–19} vibrations (vibrohaptics) to the skin of the user, or design desktop surfaces^{20–24} and multilinkage mechanisms^{25–31} to provide motion constraints. This is in stark contrast to the physical environment, in which humans feel natural objects in terms of their hardness, softness and even breaking for fragile ones through human-triggered, active touch via hands, feet or other body parts².

¹School of Engineering, Westlake University, Hangzhou, China. ²Westlake Institute for Advanced Study, Hangzhou, China. ³School of Aeronautics and Astronautics, Zhejiang University, Hangzhou, China. ⁴School for Engineering of Matter, Transport and Energy, Arizona State University, Tempe, AZ, USA.

⁵Intelligent Robot Research Center, Zhejiang Lab, Hangzhou, China. ⁶Research Center for Industries of the Future, Westlake University, Hangzhou, China.

⁷These authors contributed equally: Zhuang Zhang, Zhenghao Xu. ✉e-mail: hanqing.jiang@westlake.edu.cn

Active mechanical haptics that cover positive stiffness (feeling hardness and softness) and negative stiffness (feeling breaking and falling) are considered central to and part of the first sensory perceptions in a human's everyday interactions with the physical environment for exploring/processing information and creating an ontological metaphor^{2,32}. Currently these perceptions are missing from body-centred immersive environments. Research has shown that authentic and active mechanical haptics can lead to simultaneous physiological and psychological responses, which are difficult to trigger by visual and auditory stimuli alone^{2,33,34}. In fact, the touching sensation is remarkably different from our visual and auditory perceptions, which are passive because as humans we receive the information as third persons. The touching sensation, on the other hand, is primarily active since the interaction initiated by actively touching/holding an object creates a sense of psychological ownership, thereby generating intrapersonal and interpersonal concepts^{35,36}. Achieving a combination of visual, auditory and active touching sensory perceptions in VR/AR haptic experiences offers exciting potential for extending the realism of the virtual world.

Here we introduce the mechanisms, materials, design principles, systems integration and corresponding sensory perceptions for human-initiated, body-centred, scalable and wirelessly controlled haptic devices that are uniquely enabled by curved origami modules, allowing users to actively generate and sense mechanical touching sensations with controllable stiffness, ranging from hard to soft and from positive to negative. These active haptic mechanical devices aim to produce human-triggered mechanical sensory perception, considered one of the most indispensable human senses for interacting with the physical universe², yet rarely reproduced in the virtual world⁵. These devices are expected to enhance the VR/AR experiences beyond visual and auditory sensations while delivering a range of diverse and immersive experiences.

Figure 1a,b presents several common scenarios in our lives, of which one is that humans can easily distinguish objects when grasped in the hand or stepped on due to a distinct intrinsic property of the object, namely, its stiffness. When hitting balls or stepping on ground, human bodies feel positive stiffness, and the difference is reflected in the magnitude of the positive stiffness value. However, when crushing an egg or missing our step in walking, we experience a negative stiffness, leading to a feeling of falling and even fear. To reconstruct these active touch feelings in the VR/AR environment, we propose a curved-origami-enabled variable-stiffness module (Fig. 1c). Upon active touch/pressing, imposed by the user on this module as in the physical environment, the module will exert a corresponding reaction force, and thereby a real-time and active mechanical sensation, to the user. On the basis of the virtual scenario, the curved origami module can exert positive stiffness to simulate hardness and softness, and unprecedented negative stiffness to emulate feelings of crushing and weightlessness. Benefitting from the scalability of the origami structure^{37–44}, we further construct curved origami modules of multiple sizes using different materials (for example, plastic or steel), and then integrate them into two haptic devices for experiences, namely, an in-hand device to elicit the touching sensation and a stepping mat to generate a whole-body sensation (Fig. 1d,e). These two experiences result in more realistic sensory perceptions by successfully eliciting both the physiological and psychological reactions of users (insets), promising to deliver a highly immersive virtual experience with potential for broad applications (Fig. 1f) in entertainment, teleoperation, medical therapy and rehabilitation.

Results

Curved origami for high-range stiffness tuning

By simply introducing a circular arc-shaped cutting line characterized by an angle α that is related to the radius of the circle ρ by $\cos \alpha = b/2\rho$, where $a \times b$ is the geometry of the rectangular plate, a curved origami

is formed by folding the two-dimensional (2D) plate along the curved crease (Fig. 2a). The folding angle β in the crease is determined by the plasticity imposed by the folding process, with smaller β for larger bending deformation on the curved panels and larger β for smaller bending deformation. For the curved crease, panels and plasticity at the curved crease, a variant (non-standard) Miura origami (Fig. 2b) was used to analytically detail the mechanical behaviour of the curved origami, where angle γ is related to β , that is, $\gamma(\beta)$, which is then adopted to predict the stiffness of the curved origami and guide the design choices (see Supplementary Note 1 and Figs. 1 and 2 for details). Upon application of a vertical load on top of the origami, the curved origami exerts different force–displacement relationships depending on the competition between the bending deformation providing positive stiffness, and the folding deformation about the curved crease providing negative stiffness⁴⁵. Figure 2c presents the force–displacement relation of one curved origami defined by $\alpha = 80^\circ$ and $a/b = 1.25$ under different β (that is, initial states) for 60° , 90° and 120° , with larger β (for example, 120°) exhibiting both positive and negative ranges, while smaller β (for example, 60°) leading to only positive stiffness. Thus, for a given curved origami (that is, α), one can readily tune its stiffness by changing β , such as through a cable-driven method (Fig. 2d), where an external force is actively applied on top of the curved origami, and a cable is integrated between the two panels to adjust β from a specific initial value (for example, $\beta = 120^\circ$ for a broader tuning range) by $\Delta\beta$ in real time. In contrast to the plasticity during the folding process that defines β , the cable pulling results in an elastic folding process of the origami where it instantly recovers to its original folding state (defined by β) after the cable is released; a corresponding analytical model is also developed (Supplementary Note 1). Figure 2e shows the force–displacement relationships for a curved origami, with $\alpha = 80^\circ$, $\beta = 120^\circ$ and $a/b = 1.25$, under different cable pulling angles $\Delta\beta = 0^\circ$, 35° and 60° , exhibiting stiffness spanning positive and negative ranges. This establishes the efficacy of using a cable-driven method to tune the stiffness of curved origami in real time, with more testing data in Extended Data Fig. 1. As for haptic perceptions, different positive stiffnesses reflect levels of hardness, while negative stiffness mimics the feeling of crushing an object or of falling. Thus, during the process of actively pressing a curved origami with negative stiffness from a constant force, its acceleration becomes an essential metric for characterizing this feature. For the same curved origami in Fig. 2e under $\beta = 120^\circ$ and $\Delta\beta = 0^\circ$, 35° and 40° , the acceleration of a dead load (that is, a constant force) (Supplementary Note 2) can be as high as $0.6g$ (with $1g$ for free falling), as shown in Fig. 2f. To guide the design of the curved origami to achieve more pronounced mechanical perceptions, Fig. 2g provides the phase diagram of the absolute value of the maximum stiffness as a function of the crease angle α and tuning angle $\Delta\beta$ for a prescribed initial $\beta = 120^\circ$, that is, the actual angle with cable pulling, ranging from 0° to 120° . To harness the most pronounced stiffness perceptions, when the origami has both positive and negative stiffness ranges, only the maximum negative stiffness is chosen. When it has only the positive stiffness range, the maximum positive stiffness is adopted. From a practical perspective, α is a predetermined parameter as it defines the curved origami pattern. Consequently, this phase diagram provides a design (through α) and an operation guide (through $\Delta\beta$) to utilize curved origami for stiffness sensory perceptions. Similar to elastic deformation during cable pulling, the deformation during cyclic pressing on top of the curved origami is also elastic and shows good cyclability (Fig. 2h and Supplementary Fig. 3), in which both negative and positive stiffness can be clearly seen in each cycle.

Curved origami for active mechanical haptics

Combining the haptic perceptions generated by actively pressing the curved origami with the synchronized visual information from conventional VR devices, a highly immersive, touchable, closed-loop virtual world can be constructed, as illustrated in Fig. 3a. Here, a user can



Fig. 1 | Active stiffness perceptions in life scenarios and their reconstruction for immersive VR. **a**, Examples of human-initiated in-hand stiffness perceptions, including feeling positive stiffness when grasping elastic/rigid/soft objects, while negative stiffness when crushing readily broken objects. **b**, Examples of human-initiated body-centred stiffness perceptions, including feeling positive stiffness during stepping on varied ground, while negative stiffness when accidentally missing a step. **c**, Images of two curved origami modules for high-fidelity stiffness reconstruction. These two modules are made of different materials at different

scales, but can be tuned to have different stiffness responses using the same working principles. **d**, Present in-hand device for active touching sensation, achieving what a user sees is what the user feels. Inset: users' physiological response using the present device. **e**, Present stepping device for active whole-body sensation, achieving what a user is immersed in is what the user steps on. Inset: users' psychological response using the present device. BPM, beats per minute. **f**, Examples of potential applications, including entertainment, industrial teleoperation, psychological therapy and physical rehabilitation.

actively and physically feel what she/he sees in VR by touching or pressing motions initiated by the user through haptic devices, with curved origami as the key stiffness tuning component. The virtual scenarios (more details in Methods) act as an input to the haptic device. On the

basis of this input, β is tuned by the integrated motor in $\Delta\beta$ to simulate the expected stiffness response of what the user sees in the VR device. Thus, the user can feel the mechanical stiffness of the objects seen in the VR device in real time through active hand-grasping or through

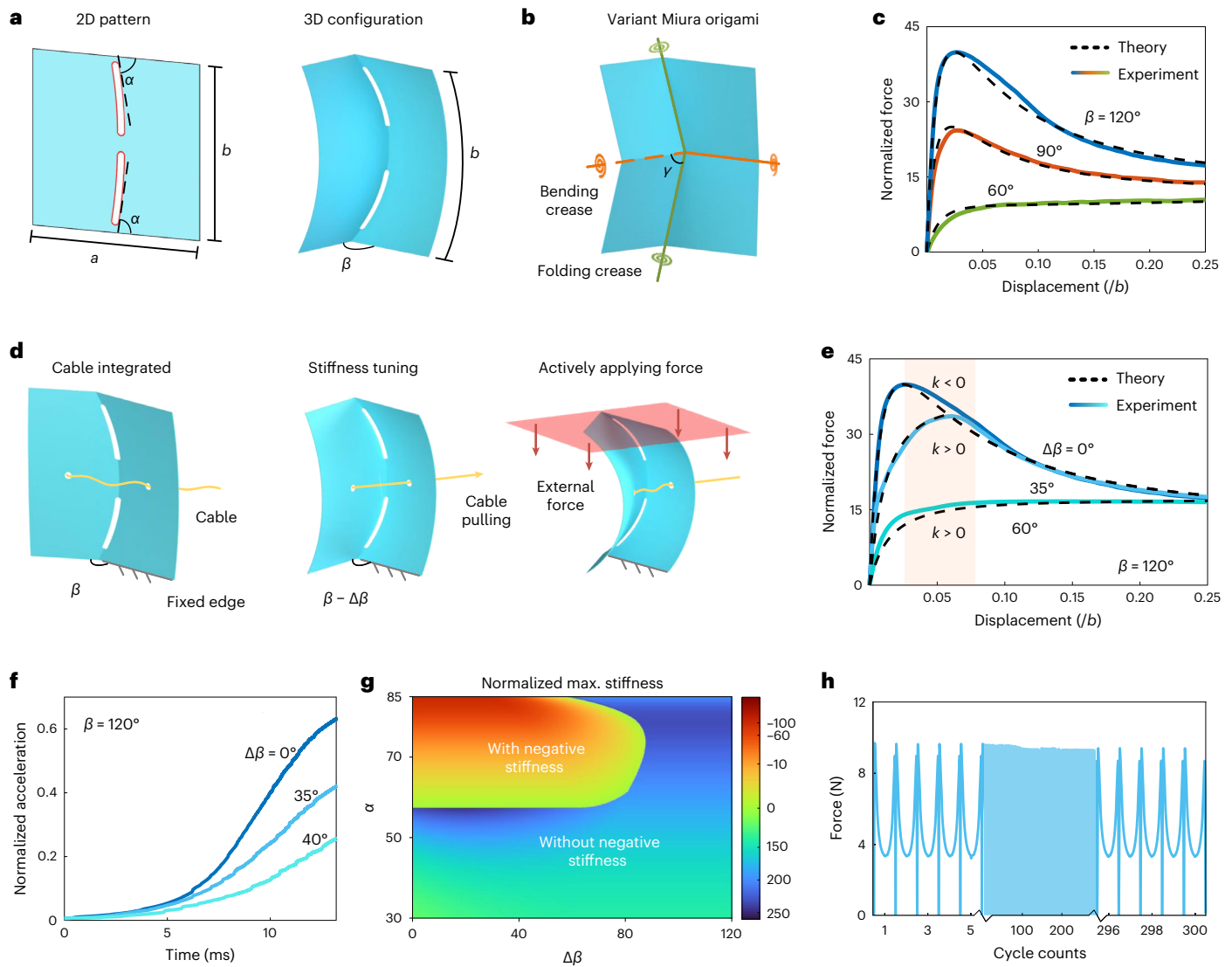


Fig. 2 | Working principle using curved origami to tune stiffness. **a**, 2D pattern and three-dimensional (3D) configuration of the curved origami module, where α , the angle between the horizontal edge and the tangent line at the end of the curved crease, denotes the normalized curvature of the crease; β , the angle between two bending panels, represents the plastic origami folding. **b**, A variant Miura origami with straight creases and rigid panels for theoretical modelling of the curved origami. The solid lines represent mountain creases, and the dashed lines represent valley creases. **c**, Force–displacement relationship of curved origami modules with different β and a fixed curve $\alpha = 80^\circ$. **d**, Working principle of the stiffness manipulation based on curved origami. Left: initial state of the origami module with an integrated cable and a fixed edge. Middle: the cable is

utilized to change the folding angle by $\Delta\beta$; Right: on actively pressing the curved origami vertically, the combined panel-bending and origami folding defines its stiffness. **e**, Force–displacement relationship of a specific module with $\alpha = 80^\circ$ and $\beta = 120^\circ$ and different $\Delta\beta$. **f**, Dropping acceleration of a dead load in a negative-stiffness domain for a specific module with $\alpha = 80^\circ$ and $\beta = 120^\circ$ and different $\Delta\beta$. **g**, Phase diagram of normalized secant stiffness for a curved origami module with a given $\beta = 120^\circ$, varying crease curvatures $30^\circ < \alpha < 85^\circ$ and cable-driven folding angles $0^\circ < \Delta\beta < 120^\circ$. The red and blue zones represent parameters with negative and positive stiffnesses, respectively. **h**, Cyclic compression test of a curved origami module, suggesting good cyclability.

body-centred, foot-stepping actions. On the other hand, the user's active interaction with the curved origami (for example, by pressing) is recorded as resistance change, which is achieved by way of silver nanowires (AgNWs) as a sensing layer deposited on the origami panel (see Methods and Extended Data Fig. 2 for details). Such changes are then converted into voltage variations using the on-board microcontroller (Fig. 3a,b and Extended Data Fig. 3). The voltage variations on the haptic device wirelessly communicate with the virtual environment engine (for example, Unity) in a personal computer and then wirelessly stream into the VR device to render necessary changes in real time, such as breaking an ice surface when the user triggers a negative stiffness (Supplementary Note 3). Figure 3c presents the relative resistance variation ($\Delta R/R_0$) of the sensing layer upon cyclic and active

pressing on top of the curved origami (with 30% nominal strain for the height change) at different folding angles ($\Delta\beta = 0^\circ, 30^\circ, 60^\circ$ and 90° for $\beta = 120^\circ$). Here two features are observed: first, the variation of the resistance has high repeatability during cyclic pressing and releasing, and second, $\Delta\beta$ shows a negligible influence, which is important for use of a universal algorithm (that is, $\Delta\beta$ -independent algorithm) to alter the virtual environment. Thus, on active human interaction, the virtual environment is changed according to the measured deformation through changes in electrical resistance. Figure 3d shows that the device possesses very stable virtual–real synchronization via its wireless transmission system. Note that the integrated motor-driven cable is only activated when the folding angle of the curved origami needs to be altered according to the virtual scenario. It then provides the various

stiffness perceptions to the user without the need for further complex control algorithms or additional actuation. Therefore, the power dissipation of about 150 mW is only produced when tuning the stiffness (Fig. 3e), leading to an energy-efficient system for human-triggered active haptics.

In-hand haptic device and stiffness perception via pressing

Here we demonstrate an object-like in-hand haptic device that provides human-triggered, active mechanical haptics with stiffness perceptions covering positive and negative ranges. The device is composed of four main subsystems (Fig. 4a, Extended Data Fig. 4 and Methods). The curved origami module connects the virtual environment and actual perceptions and achieves the ‘what a user sees is what the user feels’ (Fig. 4b) sensation by synchronously providing various stiffness perceptions based on seen virtual objects and guiding their variations in the virtual environment on the basis of active user input through pressing buttons. Figure 4c and Supplementary Video 1 demonstrate the scenarios where a user grasps various virtual objects (for example, elastic versus easily broken balls, soft versus stiff balls, with their specific stiffness values shown in Extended Data Fig. 5) and perceives their corresponding stiffness through the in-hand haptic device. The two-way connection of the curved origami between the user and virtual object renders the object in the virtual environment perceptible to the user and in turn deformable in the virtual world. This perception is triggered by the user’s active grasping, which is similar to interactions with real objects in the physical environment, thus providing an improved immersive experience.

To quantitatively evaluate the haptic perceptions empowered by the present device, 12 participants (see Methods for details) were recruited to identify four different objects of spherical shapes with distinct mechanical properties (that is, ‘rigid’ with high stiffness, ‘elastic’ with lower stiffness, ‘soft’ with the lowest stiffness and ‘crush’ with negative stiffness) using three different means: (1) virtual environment through visual information alone (that is, only VR glasses), (2) active touching alone (that is, only the present haptic device; see Extended Data Fig. 5 and Supplementary Video 2 for more details) and (3) combined information of both visual and touching (VR glasses + the present device). Figure 4d presents the confusion matrices of these three conditions, in which columns and rows correspond to the preset properties and those identified by the participants. Unsurprisingly, with only visual information from the VR glasses, the participants are unsure about the mechanical properties of the virtual objects. The highest identification rate is below 77%, and, of note, below 22% when identifying two similar objects (namely, elastic and soft). In contrast, the identification rates are almost 100% while just using the present haptic device, indicating that this device can replicate the stiffness information. Interestingly, identification rates dropped when participants used the in-hand haptic device combined with the visual information from the VR glasses, that is, over 91% for rigid and crush and just over 80% for elastic and soft, which may suggest that in terms of stiffness perception, touching is more dominant than visual information because the latter is unreliable and at times can even be misleading.

To evaluate the haptic perceptions more objectively, physiological signals from the electrical activity of the muscles (that is, electromyography (EMG)) were recorded when users tried to grasp four objects

with different stiffnesses using four different means, with one in physical and three in virtual environments. In the physical environment, four real balls with different stiffnesses were used, which formed the benchmark of the evaluation (see Methods for details). In the virtual environment, when the VR glasses visually present four balls, three means of grasping were presented: (1) using the present in-hand haptic device, (2) just a hand gesture without touching anything in the real physical world and (3) using a joystick, which is currently a common interactive tool. Figure 4e shows the r.m.s. (root mean square) values of the EMG signals on grasping various objects (real in physical world or virtual in VR world) under different in-hand conditions (see Methods and Extended Data Fig. 6 for details). The results clearly show that the present in-hand haptic device presents a very similar tendency to that based on real objects, that is, higher stiffness stimulates higher EMG voltage, and the crushing motion tends to rapidly decrease the value. In contrast, the values for just the hand gesture and the joystick are indistinguishable, lacking authentic haptic perceptions from the muscle viewpoint. A statistical analysis (Fig. 4f and Methods) further demonstrates that the present in-hand device shows significant performance ($P < 0.001$ for most) in simulating different mechanical stiffnesses when compared with real objects, providing distinguishable stiffness perceptions, while the hand gesture and the conventional joystick generate statistically insignificant perceptions ($P > 0.05$) for users.

Body-centred stepping device and whole-body perceptions

A body-centred, lower-limb-triggered stepping device integrated with larger-scale curved origami is developed to support the whole-body movement and to provide corresponding stiffness perceptions, which would further expand the immersive, active mechanical haptics beyond the hand-centred experience. The stepping device consists of four main subsystems (Fig. 5a, Extended Data Fig. 7 and Methods). The two-step transmission of the parallel worm gears and multiknotted cables enables simultaneous tuning of the stiffness of the curved origami tessellation, and generation of various closed-loop haptic perceptions. This device achieves ‘what a user is immersed in is what the user steps on’ (Fig. 5b). Figure 5c,d and Supplementary Video 3 demonstrate the scenario where a user steps on various types of virtual ground (for example, a rigid avenue versus a soft lawn versus a readily broken ice surface, whose specific stiffness values are shown in Extended Data Fig. 9) and perceives their corresponding stiffnesses through a stepping device. The two-way connection between the user and virtual environment renders the environment perceptible to the user and meanwhile reflects the user’s interaction (for example, active stepping) within the virtual world through the feedback mechanism (Extended Data Fig. 8). Among all these body-centred perceptions, falling or breaking an object (that is, crushing an ice surface, even with different thicknesses shown in Supplementary Fig. 4) is enabled by the negative stiffness, which in many cases would represent a memorable moment to the user in the virtual world, as these events normally would catch someone by surprise in the physical world.

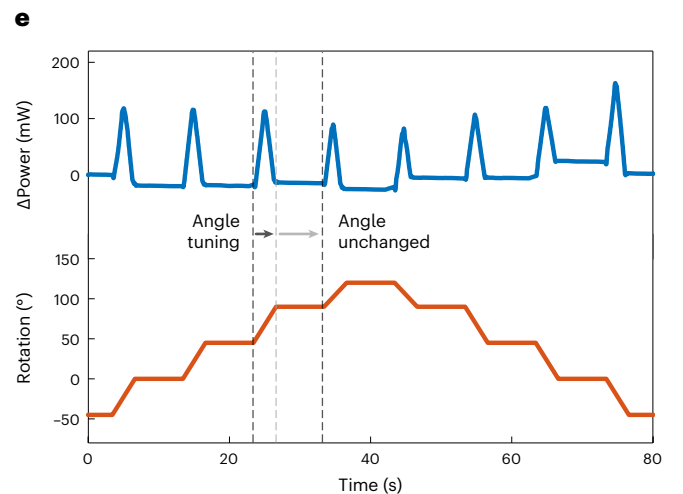
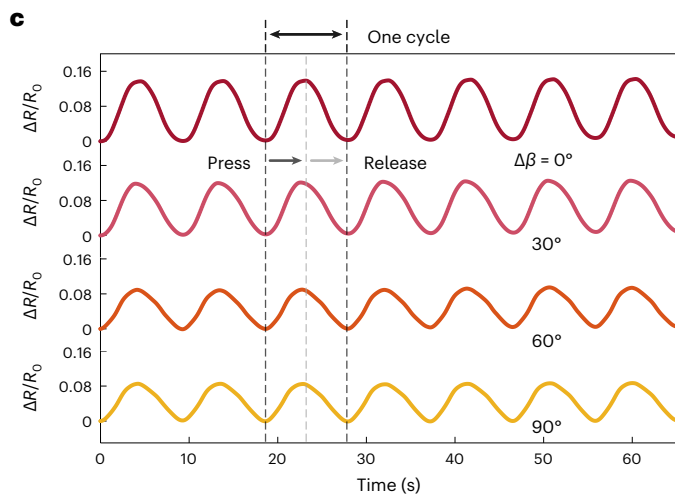
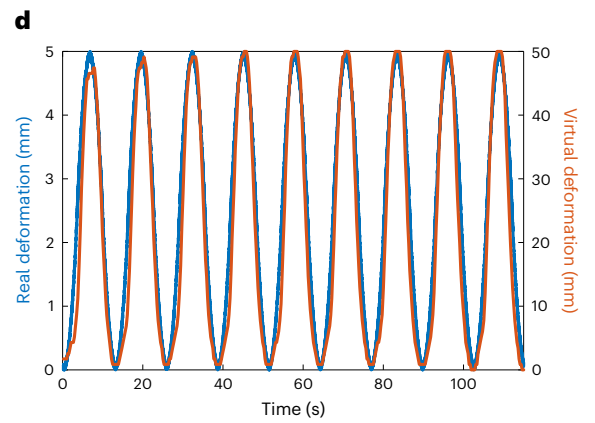
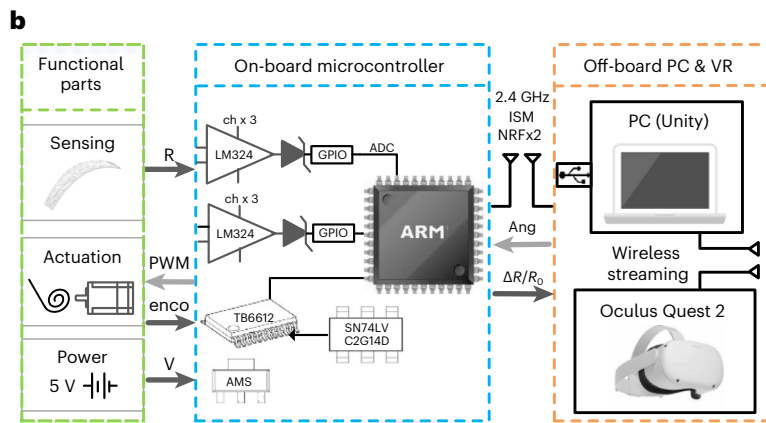
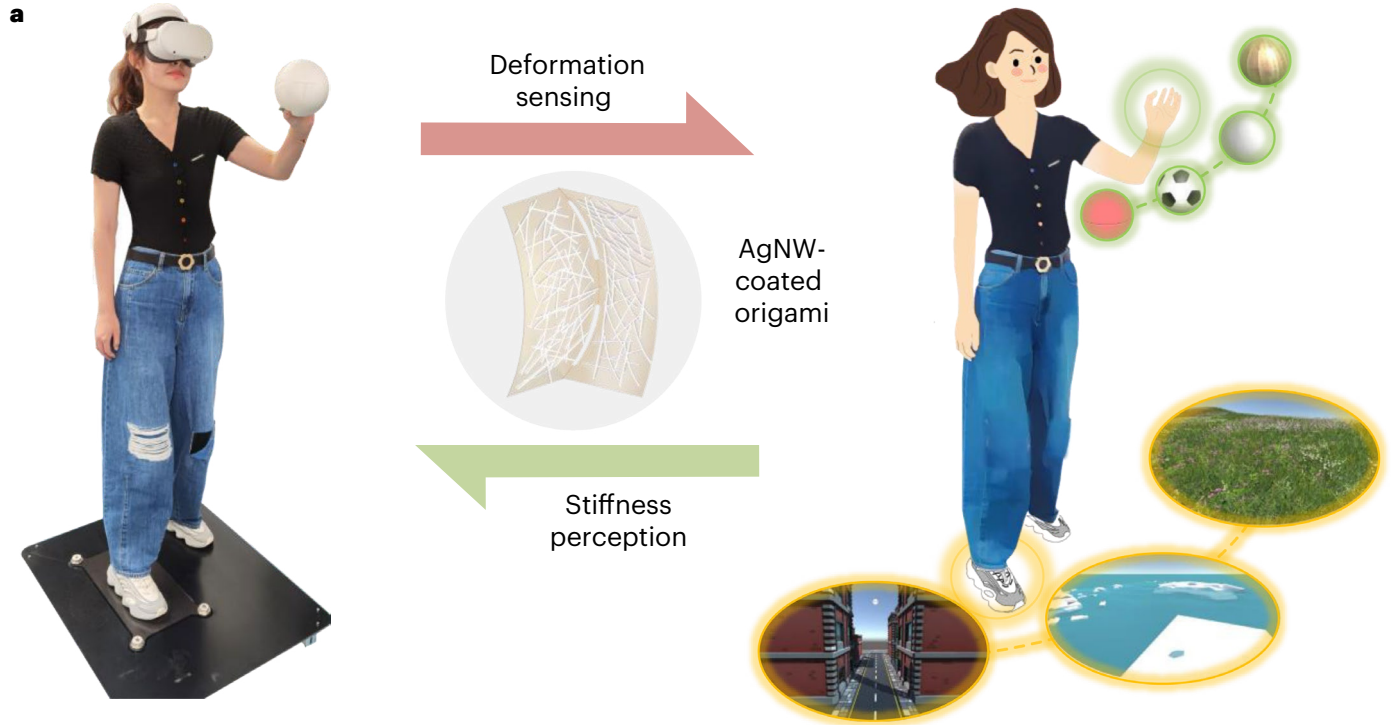
To quantitatively evaluate the body-centred haptic perceptions, 12 participants were recruited to identify four types of ground with distinct mechanical properties (that is, ‘avenue’ with high stiffness, ‘soil’ with lower stiffness, ‘grass’ with the lowest stiffness and ‘ice’ with readily triggered negative stiffness to mimic crushing) through the present

Fig. 3 | Closed-loop haptics based on curved origami. **a**, Schematics of the AgNW-coated curved origami as an interface between physical and virtual environments. **b**, System integration and circuit diagram for the haptic devices constructed with curved origami. PC, personal computer; R, measured resistance; PWM, pulse-width modulation; enco, encoder pulses; V, power supply; ch x 3, use three independent operational amplifiers to convert resistance value to voltage value; AMS, AMS1117—a series of low dropout voltage regulators; GPIO, general purpose input/output; ADC, analog to digital converter; ARM, 32-bit microcontroller based on the Cortex-M processor;

ISM, industrial scientific medical band; NRF x 2, two NRF24L01 are used for communication; Ang, folding angle of the origami. **c**, Resistance of the coated AgNW sensing layers on cyclic compressions at different folding angles of the curved origami with $\alpha = 80^\circ$ and $\beta = 120^\circ$. **d**, Deformation response of virtual objects triggered by actual deformation of the curved origami module on active cyclic compression, demonstrating a highly synchronized deformation between the physical and virtual environments bridged by the curved origami. **e**, Power consumption of the actuation system during the haptic process.

stepping device (Extended Data Fig. 9 and Supplementary Video 4). The confusion matrix (Fig. 5e) clearly shows that the identification rates for these four scenarios are all above 83%, which demonstrates that these participants can differentiate between haptic experiences using the

body-centred stepping device. To further evaluate these perceptions more objectively, we recorded the EMG signals of users' legs when they were immersed in the virtual environment via the VR glasses, and while they were stepping on the haptic device with the synchronized



stiffness as part of the virtual ground (Fig. 5f and Extended Data Fig. 10). The r.m.s. values of the EMG present a clear tendency among the three scenarios, that is, lower stiffness stimulates lower EMG voltage, and the crushing of the ice surface stimulates a similar peak voltage to the rigid avenue, wherein the former decreases rapidly, and then slows down slightly. This mixed tendency is because the EMG captures the muscle's response to both the force (rapid increase and then decrease, similar to stepping on rigid avenue) and travelling distance (slower decreasing rate, similar to stepping on soft lawn). This clearly suggests that negative stiffness created by the present curved origami can authentically simulate what the user is supposed to experience in the physical world. In addition to physiological reactions from the muscles as characterized by the EMG results, the whole-body falling and acceleration experience generated from the stepping device when the negative stiffness is triggered can stimulate psychological fluctuation. Figure 5g illustrates the heart rates of a user upon first-time steps taken on the device with three different stiffnesses according to the above three scenarios. Unlike the steady heartbeats when stepping on the rigid avenue and the soft lawn, the crushing moment of the ice surface can directly result in a rapid increase in heart rate (~15 beats per minute), and this psychological feeling of danger/fear requires several seconds to return to calm. Hence, this body-centred stepping haptic device introduces a highly immersive environment and allows the user to authentically experience sensory, physiological and psychological responses, which are common in the physical world, but rarely reproduced in the current VR/AR or existing haptic-device-powered metaverse.

Discussion

The mechanical haptics introduced here adopted delicate curved origami as a medium between the virtual and the physical environments to create human-centred, active haptic experiences with high-fidelity stiffness perceptions from positive to negative ranges. The presented mechanism shifts from existing machine-triggered, passive haptics to human-triggered interfaces that are closer to interactions with the physical universe; moreover, newly introduced negative stiffness along with various positive stiffnesses can substantially enrich the immersive experiences of users in the virtual world by reproducing the heart-racing moment when crushing objects or missing steps, as well as touching and pressing objects with different hardnesses. The working principle and characteristics have been comprehensively discussed, making the system readily replicable in conjunction with its integration strategies. Two demonstration devices (that is, in-hand device and stepping device) quantitatively validated that users can feel high-fidelity first-person sensory, physiological and psychological experiences in the constructed highly immersive virtual environment, further affirming potential for the broad-spectrum use of the device.

In addition to a leap forward in haptics by introducing a way to authentically mimic the touching sensation in the virtual environment, the present mechanical mechanism and corresponding device-level realization can find broader applications in robotics/human–robot interaction and would resolve some long-lasting challenges. For example, rehabilitation robotics⁴⁶ with the present human-initiated active haptics would extend their applications for patients with sports injuries or stroke who need to actively hold/step on objects with various stiffnesses, or patients with acrophobia who can be treated with VR exposure therapy using the body-centred stepping device to closely

mimic the physical falling sensation. Furthermore, robotics with the active touching sensation used in deep sea/planet explorations could lead to more rational decisions to the operators^{47,48}. Notably, the devices presented in this work have fixed shapes, thus a general design. Highly customized devices, such as gloves, joysticks and shoes, are also achievable by integrating smaller, customized functional parts, rendering more physical characteristics such as shape or temperature sensitivity together with their mechanical properties. Moreover, in addition to the present curved origami for generating various stiffness perceptions, other origami patterns, either deformable (for example, Kresling pattern^{40,44}) or non-deformable ones (for example, Miura pattern^{49,50}), are applicable to construct novel haptic devices exploiting their fascinating properties, such as shape-morphing, reconfigurability and multistability. Therefore, many possibilities exist to improve the performance of this system in haptics for VR in general.

Methods

Fabrication of the curved origami module

The curved origami patterns are fabricated on the basis of 2D machining and manual folding (Extended Data Fig. 2a). Many materials can be adopted to make curved origami patterns. Here, 0.2-mm-thick PET (polyethylene terephthalate) films are used for the in-hand device and 0.15-mm-thick 65 Mn spring steel sheets are used for the stepping device. The outlines and creases of the curved origami made of PET film are fabricated using a Cameo 3 cutter (Silhouette America), and those made of spring steel are manufactured through an industrial engraving machine. The initial manual folding forms the 3D configuration of the curved origami from the 2D sheets, and determines the initial β . To actively control folding angle ($\beta - \Delta\beta$ in Fig. 2) in real time for stiffness tuning, a cable is inserted through two holes on panels of the curved origami, with one side knotted behind the panel. This way the motion of the moving panel can be controlled by pulling and releasing the inserted cable, thus forming a tunable folding angle with respect to the fixed panel. An AgNW (XFNANO) suspension is utilized to form a sensing layer on the origami structure through a readily replicable coating method (Extended Data Fig. 2b). The drying process is conducted in a vacuum oven at 120 °C for 6 h. In different loading states, namely, initial state, outward bending state and inward bending state, the surface morphology of the coated AgNW layer is examined using scanning electron microscopy (SEM) (Gemini 450, Zeiss) at an operating voltage and current of 3 kV and 200 pA, respectively (Extended Data Fig. 3a). The samples are sputtered with a 3-nm-thick platinum layer before the SEM observation.

Construction of the virtual scenarios

Several 3D VR environments are designed with Unity (Unity Technologies) on a personal computer and are wirelessly projected into the VR device (Oculus Quest 2, Meta) through Oculus Air Link. The hand-tracking function of the Oculus is utilized to trace the location, orientation and gesture of the user's hands, displayed in the virtual environments. An indoor scenario is built for the demonstration of the in-hand device, with four spherical objects with different appearances on a desk. Among these four objects, the one with a wood texture is undeformable; the one with a plastic texture can be crushed when the sensing layer detects the origami deformation reaching 2 mm; the other two with a rubber texture and a football appearance are capable

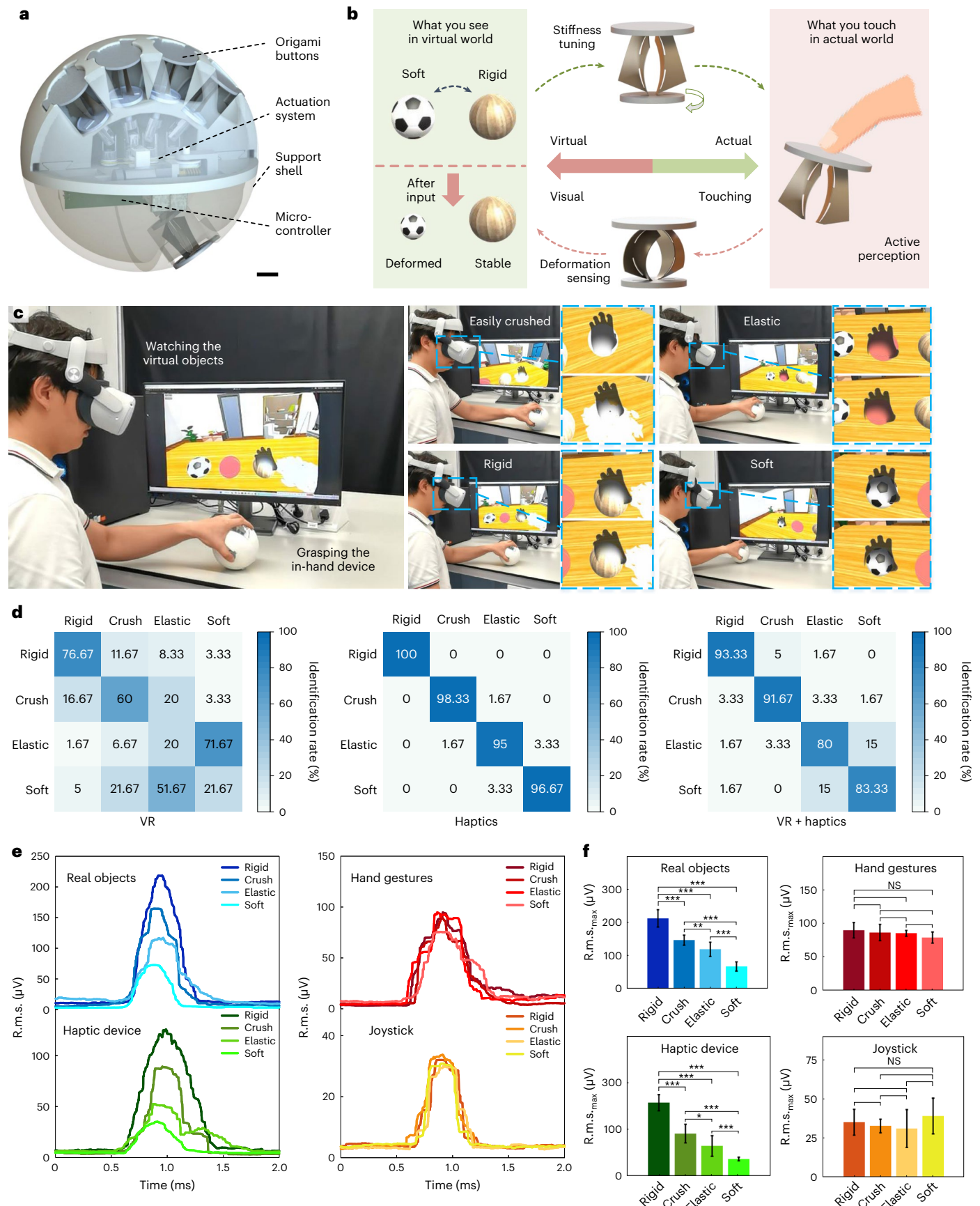
Fig. 4 | Haptic in-hand device and evaluation of its sensory perceptions.

a, Design of the in-hand haptic device with curved origami-based buttons. Scale bar, 10 mm. **b**, Schematics of the curved origami button as an interface to realize the closed-loop haptics. **c**, A user perceiving different stiffnesses of various objects in the virtual environment using the in-hand device and seeing their corresponding deformation, achieving what a user sees is what the user feels. **d**, Confusion matrices showing identification rates of 12 participants under three different interaction methods. **e**, Physiological signals (EMG) of the upper

limb when the users grasp different real objects and virtual ones under three in-hand conditions: the present haptic device, a joystick, and hand gestures alone. **f**, Evaluation of the EMG differences among the active grasps of different objects under four conditions. The statistical analysis was performed using one-way analysis of variance tests; the heights of bars represent the mean values of the samples and the error bars represent the s.d. values. The sample size of each object is 10. Asterisks denote significant effects at * $P < 0.05$, ** $P < 0.01$ and *** $P < 0.001$ (see Methods for exact P values). NS, not significant.

of volumetric change upon the resistance increase measured by the sensing layer. Three outdoor scenarios, including a city avenue, a vast lawn and an ice surface, are built for the demonstration of the stepping

device. The ground in the first two scenarios does not deform during the haptic process, while the ice surface can be crushed when the origami deformation reaches 5 mm.



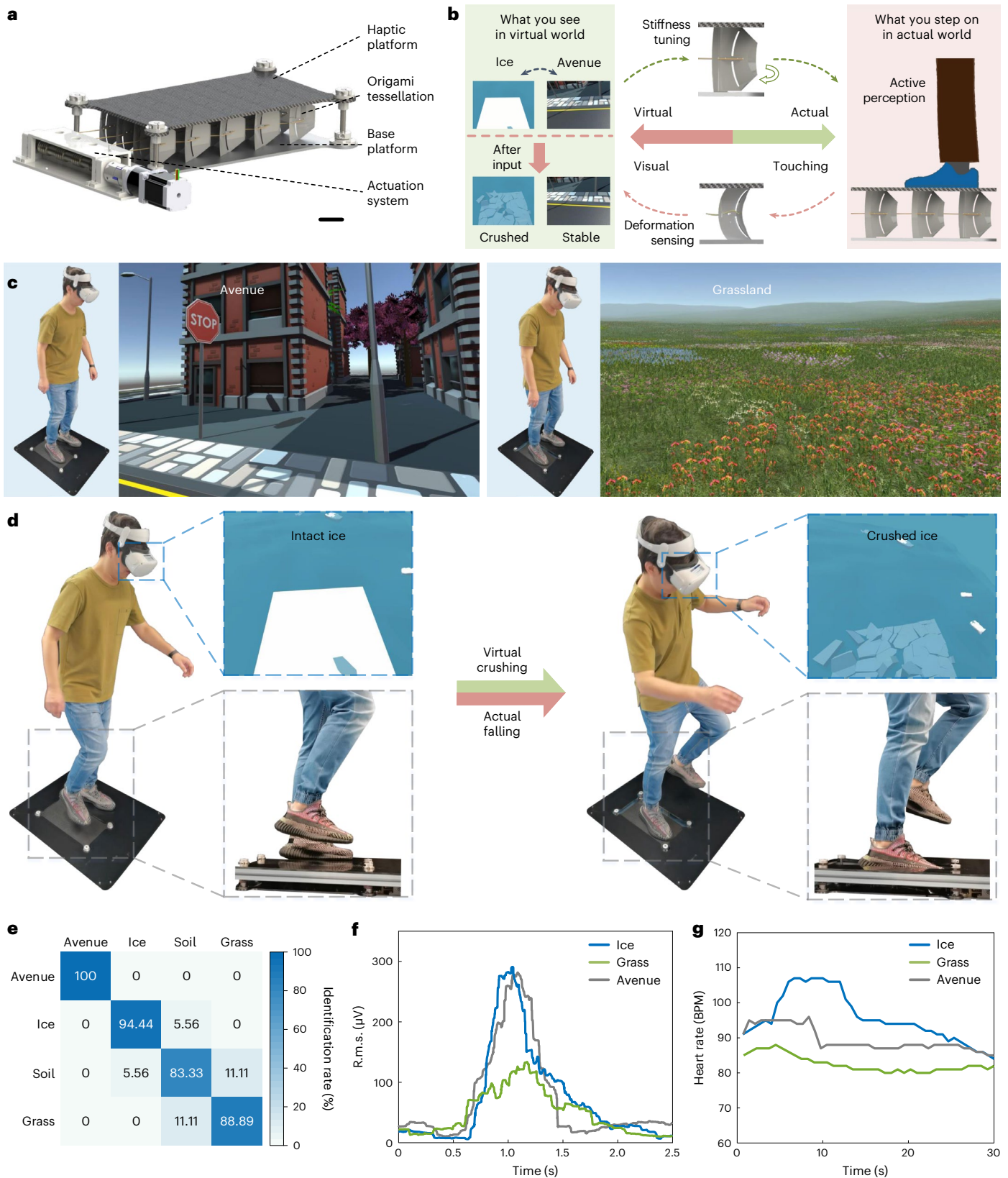


Fig. 5 | Haptic stepping device and evaluation of its sensory perceptions. **a**, Design of the stepping device with curved origami tessellations. Scale bar, 50 mm. **b**, Schematics of the curved origami as an interface to realize the closed-loop haptics. **c**, A user perceiving different stiffnesses of various types of ground in the virtual environment using the stepping device and seeing their corresponding deformation, achieving what a user is immersed in is what the user

steps on. **d**, A user capable of perceiving the sensation of falling using the present stepping device through hard stepping, synchronized by seeing a visual crushing of the ice surface in the virtual environment. **e**, Confusion matrix showing identification rates of 12 participants. **f**, Physiological signals (EMG) of the lower limb when the user steps on different virtual surfaces. **g**, Heart rates reflecting psychological reactions when the user steps on different virtual surfaces.

Characterization of the curved origami module in the haptic device

Mechanical properties. The force–displacement relationships, as well as the cyclic tests of the curved origami, are measured through uniaxial compression tests with a universal testing machine (UTM1202, Suns), under a loading speed of 4 mm min^{-1} .

Resistance. The resistance of the AgNW-coated curved origami is collected using a data acquisition system (DMM6500, Keithley). The cyclic compression and release of the origami module are achieved using a motor-driven linear lead-screw guide, with a motion range of 10 mm at four folding angles of 0° , 30° , 60° and 90° .

Deformation synchronization. The cyclic deformation of the curved origami module is achieved using a motor-driven linear lead-screw guide, and recorded through the real-time rotation measurement of the motor by a magnetic rotary encoder (AS5048A, ams-OSRAM). The linear deformation of the curved origami then can be obtained as $u = cp$, where u is the vertical deformation of the origami module, c the counts of the rotation and p the helical pinch of the lead-screw. The deformation of the virtual object is triggered by the user and calculated in the virtual environment from the resistance variation of the AgNW sensing layer, and can be displayed and recorded in Unity. A linear relationship between the real deformation of the curved origami in the physical environment and the seen (virtual) deformation of the object grasped in the virtual environment is maintained. Taking the deformation of a virtual ball with an initial diameter of 120 mm as an example, the unidirectional deformation ranges of the actual origami module and the virtual ball are 5 mm and 50 mm, respectively. In Fig. 3d, the beginning of the motor-driven deformation, as well as the recording of the deformation in both actual and virtual systems, is triggered by an identical serial port command to ensure that the starting points collapse.

Power consumption. The real-time current of the system during the stiffness tuning process is measured using a data acquisition system (DMM6500). Then, the power dissipation of the system can be calculated together with the known parameters of the input voltage and the actuation period. The in-hand haptic device with a non-optimized energy system is utilized to demonstrate this characteristic. The integrated micromotor is utilized to control the synchronous rotations of the five curved origami modules, with $\Delta\beta$ ranging from -45° to 120° .

Design and prototyping of the in-hand haptic device

Design. There are four design constraints for the in-hand device: (1) the deformation must be directly generated from the curved origami upon active pressing by the user; (2) the stiffness perception must be experienced by all five fingers, similar to most everyday grasping; (3) the in-hand device must be ergonomically friendly with a readily held shape and weight; (4) the device must be untethered to avoid users being restricted by the wires. Following these constraints, a spherical in-hand device with five synchronously controlled origami buttons is designed with the following four subsystems (Fig. 4a and Extended Data Fig. 4a): (1) five buttons constructed with curved origami for virtual–physical environment feedback generation on the user's active pressing; (2) an actuation system to tune the stiffness of the curved origami by transmitting the motor rotation to the action of cable pulling/releasing; (3) electronic control components for the feedback loop (that is, stiffness tuning, actuation, sensing) and wireless transmission; (4) a support shell for housing the buttons according to finger position, electronics and ergonomic considerations for human grasping action. Five curved origami buttons are positioned on the spherical supporting shell according to the common gesture of human grasping, with their fixed bottom plates connected with the actuation system and moving plates on the top constrained by the slide guide for users' active grasping. Constrained by the housing

space of the origami buttons, the cable is not directly inserted inside the origami structures. Instead, relative rotations between the fixed (top) and moving (bottom) plates of the origami buttons are adopted to control the folding angles for stiffness tuning (Extended Data Fig. 5), which is further achieved through a SI-MO (single input–multiple output) actuation strategy constructed on the basis of cable routing (Extended Data Fig. 4b,c). Given that the vertical directions of the five buttons are neither parallel nor coplanar, four rollers with axes parallel to the cable spool are designed for planar cable routing and connected with the five origami buttons through universal joints. To save space, the buttons for the thumb and middle finger are connected with an identical roller. This way, rotations of the bottom plates of the five origami buttons can be synchronously controlled by one micromotor, leading to a more compact and lightweight structure. Here, worm gears are utilized to transmit the rotation from the micromotor to the cable spool. Due to the self-locking characteristics of the worm gears, this structure withstands the torque of the relative rotations between the top and bottom plates of the curved origami and maintains states of prescribed stiffness, rendering a more energy-efficient system. In addition to these mechanical components, electronic control components including an on-board microcontroller (Fig. 3b, Supplementary Note 3 and Supplementary Figs. 5–8) and a small 5 V battery are integrated into the hollow supporting shell, to realize untethered control.

Prototyping. The supporting shells and the cable rollers are 3D printed with photosensitive resin (Somos Imagine 8000 and Somos WaterClear Ultra 10122, DSM Desotech) through an SLA (stereo lithography appearance) 3D printer (Lite 800, UnionTech). The fixed (bottom) and moving (top) plates of the origami buttons are 3D printed with polylactic acid (eSilk-PLA, eSUN) through an FDM (fused deposition modelling) 3D printer (Pro3 plus, Raise3D). The cable is made of Kevlar with a diameter of 0.8 mm. The universal joints, bearings and worm gears are standard metal parts. The weight of the current in-hand device is around 600 g, in which the 3D-printed solid support shell makes up about 70% of the total weight. It should be noted that currently there is no lightweight optimization. It is believed that the weight can be substantially reduced by designing hollow support structures.

Design and prototyping of the stepping device

Design. There are four design constraints for the stepping device: (1) the deformation must be directly generated from the curved origami upon active stepping by the user; (2) the stiffness perception must be experienced with a body-level motion, similar to most everyday walking; (3) the stepping device must be capable of supporting the weight of an adult in high-stiffness state and readily deformed in low-stiffness state; (4) the moving platform of the stepping device must have only one degree of freedom (vertical) to ensure haptic safety. Following these constraints, a stepping device with a flat, vertically deformable haptic platform and synchronously controlled curved origami tessellation is designed (Fig. 5a and Extended Data Fig. 7a) with four main subsystems: (1) a moving platform for stepping interaction; (2) a curved origami tessellation for supporting the user's weight and feedback generation upon active stepping; (3) a base platform for locating origami tessellation and supporting the whole structure; (4) an actuation system to tune the stiffness of the curved origami by transmitting the motor rotation to the origami folding through cables. Four cylindrical guides and the corresponding linear bearings are fixed on the base and haptic platforms, respectively, constraining the motion of the haptic platform only in the vertical direction on active stepping of the user. A two-stage transmission system consisting of a multihead worm gear transmission and multiknotted cable-driven transmissions is designed, where the former transmits the rotation from the motor to the four gears to simultaneously pull four independent cables, and the latter converts each cable pull to simultaneous folding of five curved origami modules through five knots evenly located behind the five moving

panels (Extended Data Fig. 7b,c). This way, simultaneous control of the origami tessellation with 20 modules located in a 4×5 matrix can be achieved through only one motor (Extended Data Fig. 7d), forming an easily manipulated, energy-efficient actuation system similar to that of the in-hand device.

Prototyping. The haptic platform is made of a 5-mm-thick carbon fibre plate, 2D manufactured through an industrial engraving machine. The base platform made of aluminium alloy is manufactured through computer numerical control machining. The pulling cable is made of Kevlar with a diameter of 0.8 mm. The coupling, bearings and cylindrical guides are standard metal parts. Other structural parts are 3D printed with polylactic acid (PLA+, eSUN) through an FDM 3D printer (Pro3 plus).

Stiffness perception evaluation

To evaluate the high-fidelity stiffness perception generated from the present in-hand and stepping devices, two experiments were conducted to record the identification rates of the different stiffnesses perceived by the users. Twelve healthy 22- to 35-year-old participants (nine males and three females) took part in these experiments. For the experiments with the in-hand device, each participant was first told that there are four different objects with distinct mechanical properties (that is, rigid, elastic, soft and crush), then asked to indicate the corresponding properties of the four virtual objects in VR, on the basis of only visual information without touching. After this, the participant was asked to take off the VR glasses and indicate the four properties solely using the present haptic device. Finally, the participant was asked to put on the VR glasses again and indicate the properties under the combined visual and touching information from both the VR glasses and the present haptic device. The tests under each condition were randomly applied and recorded five times. For the experiments on the stepping device, each participant was first told that there are four types of ground with distinct mechanical properties (that is, avenue, soil, grass and ice), then asked to indicate the corresponding properties of the four simulated types of ground through active stepping on the present stepping device. The tests under each condition were randomly applied and recorded three times. All subjects provided informed consent before the tests. All experiments on humans (including the physiological one in the following) were approved by the Ethics Committee of Westlake University (no. 20220621JHQ001 and no. 20220721JHQ001).

Physiological experiment

EMG measurement. To characterize the variation of the electrical activity of the muscles on different stiffness perceptions, a wireless EMG sensor (Pico EMG, Cometa Systems) was utilized to record the action voltages during active haptics. For the experiments with the in-hand device, the participant was first asked to grasp four real balls (a rigid wooden ball, an easily buckled plastic ball, an elastic no. 1 soccer ball with higher pressure and a soft no. 1 soccer ball with lower pressure) in the physical environment, which serves as the benchmark of the evaluation. Later, the participant was asked to put on the VR glasses, with a virtual scenario containing four different spherical objects, then grasp them through the present in-hand device, hand gestures alone and a conventional joystick. The grasping of each object under each condition was repeated ten times, with the EMG sensor attached on the middle surface of the extensor digitorum (Supplementary Fig. 9a). For the experiments with the stepping device, the participant was asked to step on the stepping device with three simulated types of ground (that is, avenue, grass and ice). The stepping on each simulated type was repeated ten times, with the EMG sensor attached on the surface of the gastrocnemius muscle (Supplementary Fig. 9b).

Heart-rate measurement. To characterize the psychological changes in the participant when experiencing various simulated types of

ground, an electrocardiography sensor (PC-80B, Heal Force) was utilized to record the heart rate during active stepping (Supplementary Fig. 10). The participant was asked to finish his/her first-time step on the device with three simulated types of ground (that is, avenue, grass and ice).

Data analysis and statistics. All data were analysed using the available built-in functions of MATLAB (R2021b, MathWorks) and were processed using Origin (2021, OriginLab). All data are reported as mean values with s.d. when indicated (Fig. 4f). In the statistical analyses of standardized tests, the factor (independent variable) is the stiffness of the object; the dependent variable is the maximum r.m.s. value of the EMG collected, on the middle surface of the extensor digitorum for the in-hand haptic device, or on the surface of the gastrocnemius muscle for the stepping device. All data were demonstrated to be normally distributed, determined using the Kolmogorov–Smirnov test ($P > 0.05$) before analysis for statistical significance. One-way analysis of variance was used to statistically analyse the significant influences of stiffness perceptions on the r.m.s. values of the EMG. The P values between the four real objects in Fig. 4f are 7.37×10^{-12} , 6.03×10^{-8} , 1.71×10^{-6} , 3.84×10^{-10} , 3.70×10^{-3} and 4.54×10^{-6} , from top to bottom of the figure. For the developed haptic device, the P values are 2.22×10^{-14} , 4.30×10^{-9} , 1.73×10^{-7} , 4.22×10^{-7} , 2.65×10^{-2} and 9.34×10^{-4} . For the hand gestures, the P values are 0.186, 0.603, 0.691, 0.389, 0.901 and 0.474. For the joystick, the P values are 0.388, 0.118, 0.146, 0.394, 0.689 and 0.429. According to the results of one-way analysis of variance, there is a significant difference when grasping four real balls and the present in-hand device with four different stiffness states; however, no significant difference is found when using joysticks or hand gestures.

Reporting summary

Further information on research design is available in the Nature Portfolio Reporting Summary linked to this article.

Data availability

All data needed to evaluate the conclusions in the papers are present in the Article and/or the Supplementary Information. The data collected during the experiment with the volunteers can be downloaded from <https://github.com/EMLQ/AMH>. The data are available via Zenodo at <https://doi.org/10.5281/zenodo.7789004> (ref. 51).

Code availability

The code that supports the active mechanical haptic system within this paper and other findings of this study are available from <https://github.com/EMLQ/AMH>. The code is available via Zenodo at <https://doi.org/10.5281/zenodo.7789004> (ref. 51).

References

1. Sparkes, M. What is a metaverse. *New Sci.* **251**, 18 (2021).
2. Ackerman, J. M., Nocera, C. C. & Bargh, J. A. Incidental haptic sensations influence social judgments and decisions. *Science* **328**, 1712–1715 (2010).
3. Yu, X. et al. Skin-integrated wireless haptic interfaces for virtual and augmented reality. *Nature* **575**, 473–479 (2019).
4. Biswas, S. & Visell, Y. Haptic perception, mechanics, and material technologies for virtual reality. *Adv. Funct. Mater.* **31**, 2008186 (2021).
5. Pyun, K. R., Rogers, J. A. & Ko, S. H. Materials and devices for immersive virtual reality. *Nat. Rev. Mater.* **7**, 841–843 (2022).
6. Li, S., Bai, H., Shepherd, R. F. & Zhao, H. Bio-inspired design and additive manufacturing of soft materials, machines, robots, and haptic interfaces. *Angew. Chem. Int. Ed.* **58**, 11182–11204 (2019).
7. Jung, Y. H., Kim, J.-H. & Rogers, J. A. Skin-integrated vibrotactile interfaces for virtual and augmented reality. *Adv. Funct. Mater.* **31**, 2008805 (2021).

8. Zhu, M. L. et al. Haptic-feedback smart glove as a creative human-machine interface (HMI) for virtual/augmented reality applications. *Sci. Adv.* **6**, eaaz8693 (2020).
9. Liu, Y. et al. Electronic skin as wireless human-machine interfaces for robotic VR. *Sci. Adv.* **8**, eabl6700 (2022).
10. Jung, Y. H. et al. A wireless haptic interface for programmable patterns of touch across large areas of the skin. *Nat. Electron.* **5**, 374–385 (2022).
11. Sun, Z., Zhu, M., Shan, X. & Lee, C. Augmented tactile-perception and haptic-feedback rings as human-machine interfaces aiming for immersive interactions. *Nat. Commun.* **13**, 5224 (2022).
12. Kim, D. et al. Actuating compact wearable augmented reality devices by multifunctional artificial muscle. *Nat. Commun.* **13**, 4155 (2022).
13. Choi, I., Ofek, E., Benko, H., Sinclair, M. & Holz, C. CLAW: a multifunctional handheld haptic controller for grasping, touching, and triggering in virtual reality. In *CHI '18: Proc. 2018 CHI Conference on Human Factors in Computing Systems* 654 (Association for Computing Machinery, 2018).
14. Scheggi, S., Meli, L., Pacchierotti, C. & Prattichizzo, D. Touch the virtual reality: using the leap motion controller for hand tracking and wearable tactile devices for immersive haptic rendering. In *ACM SIGGRAPH 2015 Posters* 31 (Association for Computing Machinery, 2015).
15. Giraud, F. H., Joshi, S. & Paik, J. Haptigami: a fingertip haptic interface with vibrotactile and 3-DoF cutaneous force feedback. *IEEE Trans. Haptics* **15**, 131–141 (2022).
16. Pezent, E., Agarwal, P., Hartcher-O'Brien, J., Colonnese, N. & O'Malley, M. K. Design, control, and psychophysics of Tasbi: a force-controlled multimodal haptic bracelet. *IEEE Trans. Robot.* **38**, 2962–2978 (2022).
17. Yao, K. M. et al. Encoding of tactile information in hand via skin-integrated wireless haptic interface. *Nat. Mach. Intell.* **4**, 893–903 (2022).
18. Leroy, E., Hinchet, R. & Shea, H. Multimode hydraulically amplified electrostatic actuators for wearable haptics. *Adv. Mater.* **32**, 2002564 (2020).
19. Chinello, F., Pacchierotti, C., Malvezzi, M. & Prattichizzo, D. A three revolutes-revolutes-spherical wearable fingertip cutaneous device for stiffness rendering. *IEEE Trans. Haptics* **11**, 39–50 (2018).
20. Xu, H., Peshkin, M. A. & Colgate, J. E. UltraShiver: lateral force feedback on a bare fingertip via ultrasonic oscillation and electroadhesion. *IEEE Trans. Haptics* **12**, 497–507 (2019).
21. Steed, A., Ofek, E., Sinclair, M. & Gonzalez-Franco, M. A mechatronic shape display based on auxetic materials. *Nat. Commun.* **12**, 4758 (2021).
22. Peng, Y. et al. Elastohydrodynamic friction of robotic and human fingers on soft micropatterned substrates. *Nat. Mater.* **20**, 1707–1711 (2021).
23. Choi, C. et al. Surface haptic rendering of virtual shapes through change in surface temperature. *Sci. Robot.* **7**, eabl4543 (2022).
24. Li, X. et al. Nanotexture shape and surface energy impact on electroadhesive human-machine interface performance. *Adv. Mater.* **33**, 2008337 (2021).
25. Mintchev, S., Salerno, M., Cherpillod, A., Scaduto, S. & Paik, J. A portable three-degrees-of-freedom force feedback origami robot for human-robot interactions. *Nat. Mach. Intell.* **1**, 584–593 (2019).
26. Pacchierotti, C. et al. Wearable haptic systems for the fingertip and the hand: taxonomy, review, and perspectives. *IEEE Trans. Haptics* **10**, 580–600 (2017).
27. Xiong, Q. et al. So-EAGlove: VR haptic glove rendering softness sensation with force-tunable electrostatic adhesive brakes. *IEEE Trans. Robot.* **38**, 3450–3462 (2022).
28. Giri, G. S., Maddahi, Y. & Zareinia, K. An application-based review of haptics technology. *Robotics* **10**, 29 (2021).
29. Choi, I., Hawkes, E. W., Christensen, D. L., Ploch, C. J. & Follmer, S. Wolverine: a wearable haptic interface for grasping in virtual reality. In *2016 IEEE/RSJ International Conference on Intelligent Robots and Systems (IROS 2016)* 986–993 (IEEE, 2016).
30. Martinez, M. O. et al. Open source, modular, customizable, 3-D printed kinesthetic haptic devices. In *2017 IEEE World Haptics Conference (WHC)* 142–147 (IEEE, 2017).
31. Jadhav, S., Majit, M. R. A., Shih, B., Schulze, J. P. & Tolley, M. T. Variable stiffness devices using fiber jamming for application in soft robotics and wearable haptics. *Soft Robot.* **9**, 173–186 (2022).
32. Ernst, M. O. & Banks, M. S. Humans integrate visual and haptic information in a statistically optimal fashion. *Nature* **415**, 429–433 (2002).
33. Moscatelli, A. et al. Touch as an auxiliary proprioceptive cue for movement control. *Sci. Adv.* **5**, eaaw3121 (2019).
34. Kieliba, P., Clode, D., Maimon-Mor, R. O. & Makin, T. R. Robotic hand augmentation drives changes in neural body representation. *Sci. Robot.* **6**, eabd7935 (2021).
35. Peck, J. & Shu, S. B. The effect of mere touch on perceived ownership. *J. Consum. Res.* **36**, 434–447 (2009).
36. Brasel, S. A. & Gips, J. Tablets, touchscreens, and touchpads: how varying touch interfaces trigger psychological ownership and endowment. *J. Consum. Psychol.* **24**, 226–233 (2014).
37. Felton, S. Origami for the everyday. *Nat. Mach. Intell.* **1**, 555–556 (2019).
38. Rus, D. & Tolley, M. T. Design, fabrication and control of origami robots. *Nat. Rev. Mater.* **3**, 101–112 (2018).
39. Hawkes, E. et al. Programmable matter by folding. *Proc. Natl Acad. Sci. USA* **107**, 12441–12445 (2010).
40. Zhai, Z., Wang, Y. & Jiang, H. Origami-inspired, on-demand deployable and collapsible mechanical metamaterials with tunable stiffness. *Proc. Natl Acad. Sci. USA* **115**, 2032–2037 (2018).
41. Melancon, D., Gorissen, B., Garcia-Mora, C. J., Hoberman, C. & Bertoldi, K. Multistable inflatable origami structures at the metre scale. *Nature* **592**, 545–550 (2021).
42. Felton, S., Tolley, M., Demaine, E., Rus, D. & Wood, R. A method for building self-folding machines. *Science* **345**, 644–646 (2014).
43. Faber, J. A., Arrieta, A. F. & Studart, A. R. Bioinspired spring origami. *Science* **359**, 1386–1391 (2018).
44. Wu, S. et al. Stretchable origami robotic arm with omnidirectional bending and twisting. *Proc. Natl Acad. Sci. USA* **118**, e2110023118 (2021).
45. Zhai, Z., Wang, Y., Lin, K., Wu, L. & Jiang, H. In situ stiffness manipulation using elegant curved origami. *Sci. Adv.* **6**, eabe2000 (2020).
46. Su, H. et al. Physical human-robot interaction for clinical care in infectious environments. *Nat. Mach. Intell.* **3**, 184–186 (2021).
47. Li, G. et al. Self-powered soft robot in the Mariana Trench. *Nature* **591**, 66–71 (2021).
48. Panzirsch, M. et al. Exploring planet geology through force-feedback telemanipulation from orbit. *Sci. Robot.* **7**, eabl6307 (2022).
49. Liu, K., Pratapa, P. P., Misseroni, D., Tachi, T. & Paulino, G. H. Triclinic metamaterials by tristable origami with reprogrammable frustration. *Adv. Mater.* **34**, 2107998 (2022).
50. Song, Z. et al. Origami lithium-ion batteries. *Nat. Commun.* **5**, 3140 (2014).
51. Zhang, Z. et al. Active mechanical haptics with high-fidelity perceptions for immersive virtual reality. *Zenodo* <https://doi.org/10.5281/zenodo.7789004> (2023).

Acknowledgements

We thank the Research Center for Industries of the Future (RCIF) at Westlake University and Westlake Education Foundation for

supporting this work. Z. Zhang acknowledges support from the National Natural Science Foundations of China (grant 52205031). Y.W. acknowledges support from the National Natural Science Foundation of China (grants 11872328 and 12132013). L.K. acknowledges support from the Key Project of Zhejiang Lab (G2021NB0AL03) and the National Natural Science Foundations of China (grant 52205034). We also thank Y. Jiang for helping with human experiments and data analysis, and Y. Huang for helping with the design of the electronic and control system.

Author contributions

Z. Zhang, Z.X. and H.J. developed the concept. Z. Zhang, Z.X., L.E. and P.W. designed and prototyped the devices. Z. Zhang and L.E. developed the electronics, the control system and the software. Z. Zhang, Z.X., L.E., P.W., S.C., Z. Zhai, Y.W. and H.J. carried out experiments and analysis. Z. Zhang, Z.X., L.E. and L.K. collected the user data. Z. Zhang, Z.X. and H.J. wrote the manuscript.

Competing interests

The authors declare no competing interests.

Additional information

Extended data is available for this paper at <https://doi.org/10.1038/s42256-023-00671-z>.

Supplementary information The online version contains supplementary material available at <https://doi.org/10.1038/s42256-023-00671-z>.

Correspondence and requests for materials should be addressed to Hanqing Jiang.

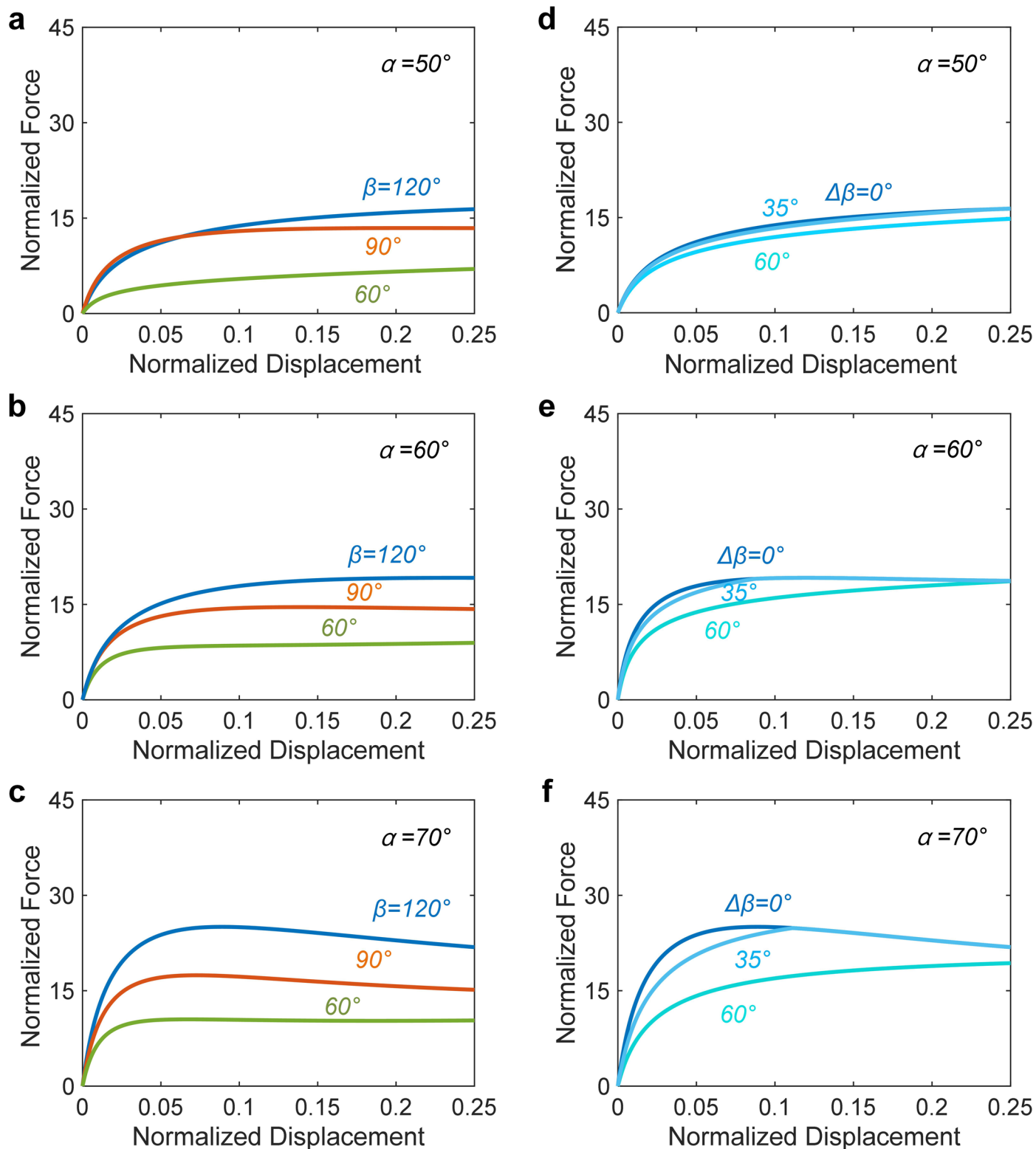
Peer review information *Nature Machine Intelligence* thanks Xinge Yu and the other, anonymous, reviewer(s) for their contribution to the peer review of this work.

Reprints and permissions information is available at www.nature.com/reprints.

Publisher's note Springer Nature remains neutral with regard to jurisdictional claims in published maps and institutional affiliations.

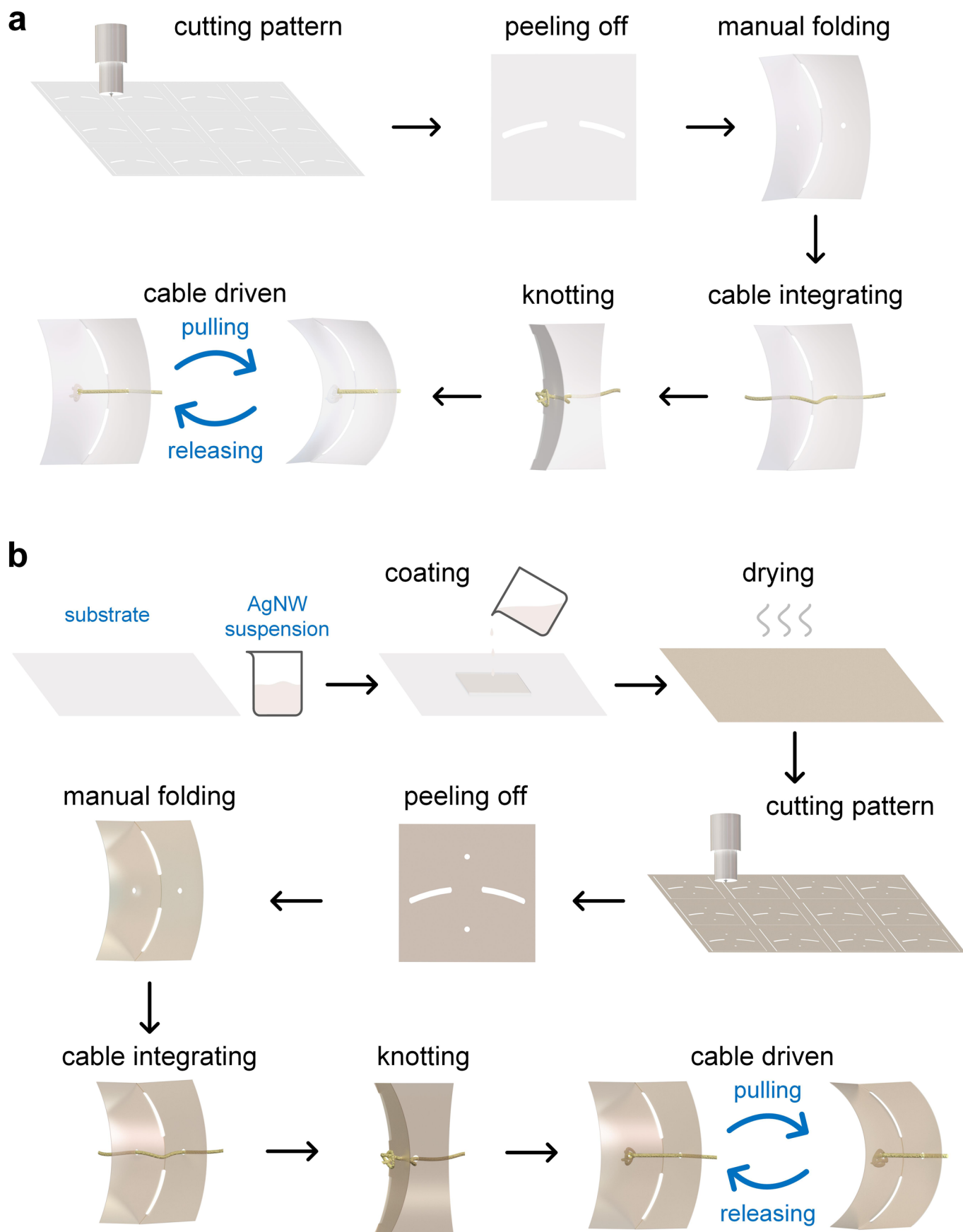
Springer Nature or its licensor (e.g. a society or other partner) holds exclusive rights to this article under a publishing agreement with the author(s) or other rightsholder(s); author self-archiving of the accepted manuscript version of this article is solely governed by the terms of such publishing agreement and applicable law.

© The Author(s), under exclusive licence to Springer Nature Limited 2023



Extended Data Fig. 1 | Some force–displacement relationships of curved origami modules with different angles α . **a–c**, normalized force–displacement relationship of curved origami modules with different initial folding angles β

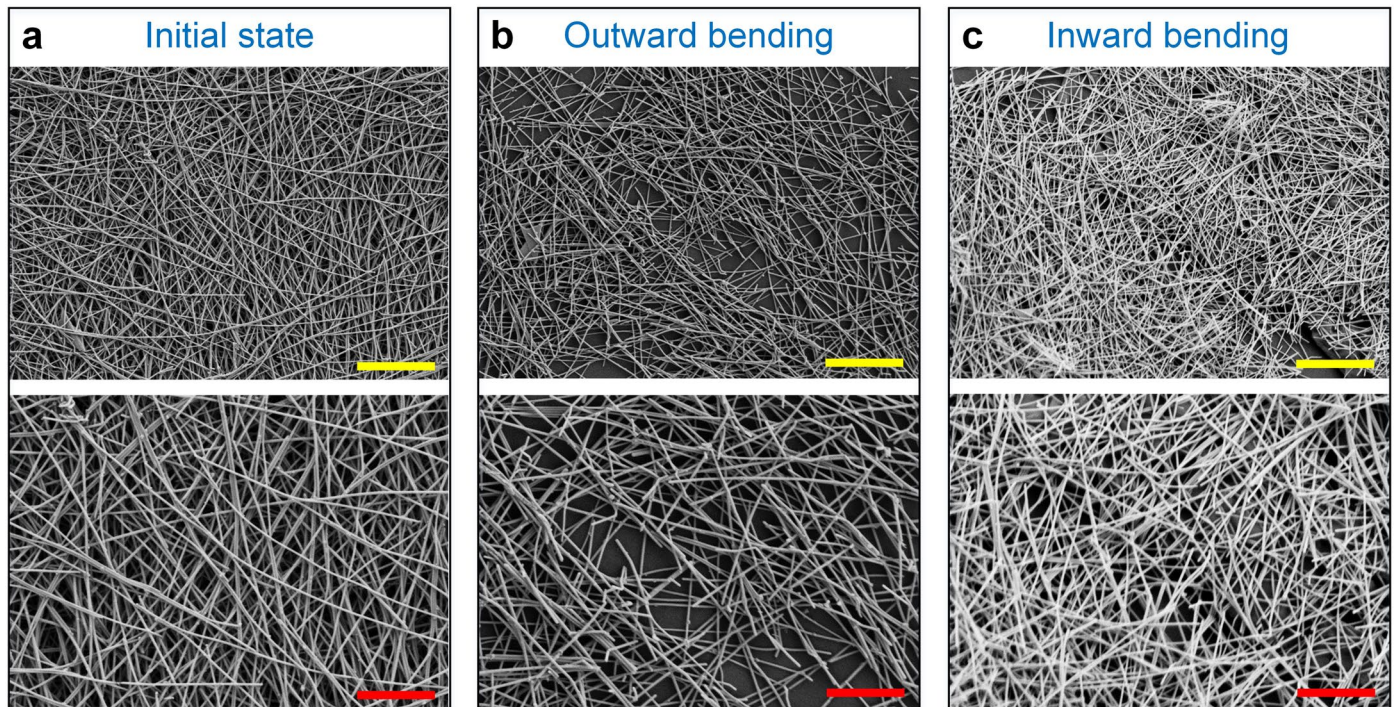
with angles $\alpha = 50^\circ, 60^\circ, 70^\circ$. **d–f**, normalized force–displacement relationship of curved origami modules with fixed initial folding angles $\beta = 120^\circ$ and different controllable angles $\Delta\beta$, with different angles $\alpha = 50^\circ, 60^\circ, 70^\circ$.



Extended Data Fig. 2 | See next page for caption.

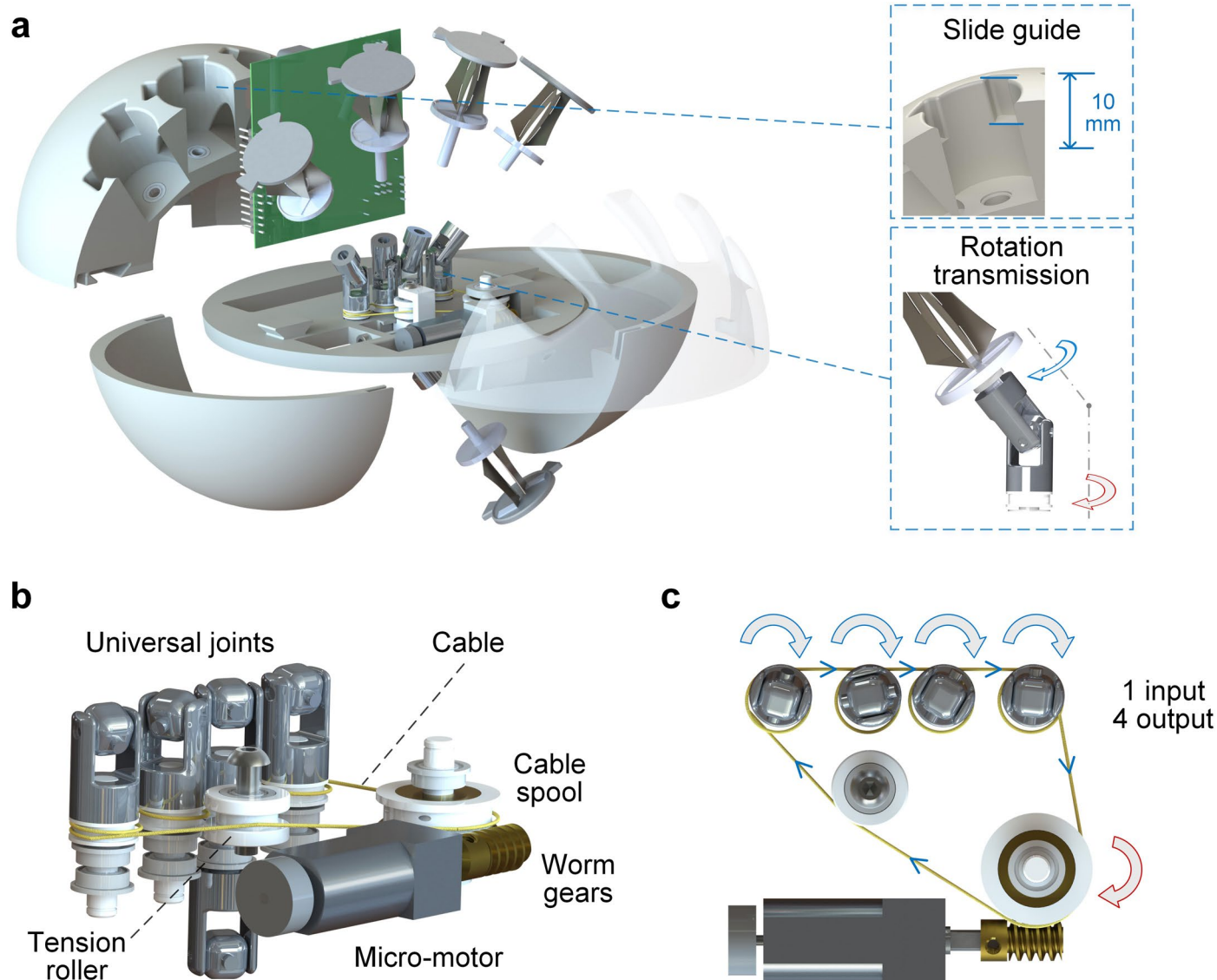
Extended Data Fig. 2 | Fabrication of the curved origami. **a**, Fabrication of curved origami using plastic or metal materials: step a1, sheets cutting according to the 2D curved origami pattern, using an engraving machine; step a2, peel off the origami patterns from the substrate; step a3, manually fold the 2D pattern along the curved crease to form the 3D configuration with bending panels; step a4, integrate a cable through two holes on the panels; step a5, knotting the cable behind one side of the origami panel to form motion constraint; step a6, pull

and release the cable to control the curved origami folding. **b**, Fabrication of the curved origami with the silver nanowires (AgNWs) coated layer for sensing: step b1, prepare the substrate and AgNWs suspension; step b2, pour the AgNWs suspension onto the surface of the substrate; step b3, dry the suspension in the oven for 6 hours to obtain the AgNWs-coated substrate; steps b4-b9, similar fabrication process with steps a1-a6.



Extended Data Fig. 3 | SEM images of the AgNWs-coated origami. SEM images of AgNWs coated on the surface of a PET film under initial (a), outward (b), and inward (c) bending at low (up) and high (bottom) magnitude. The scale bars are $2\ \mu\text{m}$ (in yellow) and $1\ \mu\text{m}$ (in red), respectively. Outward bending shows

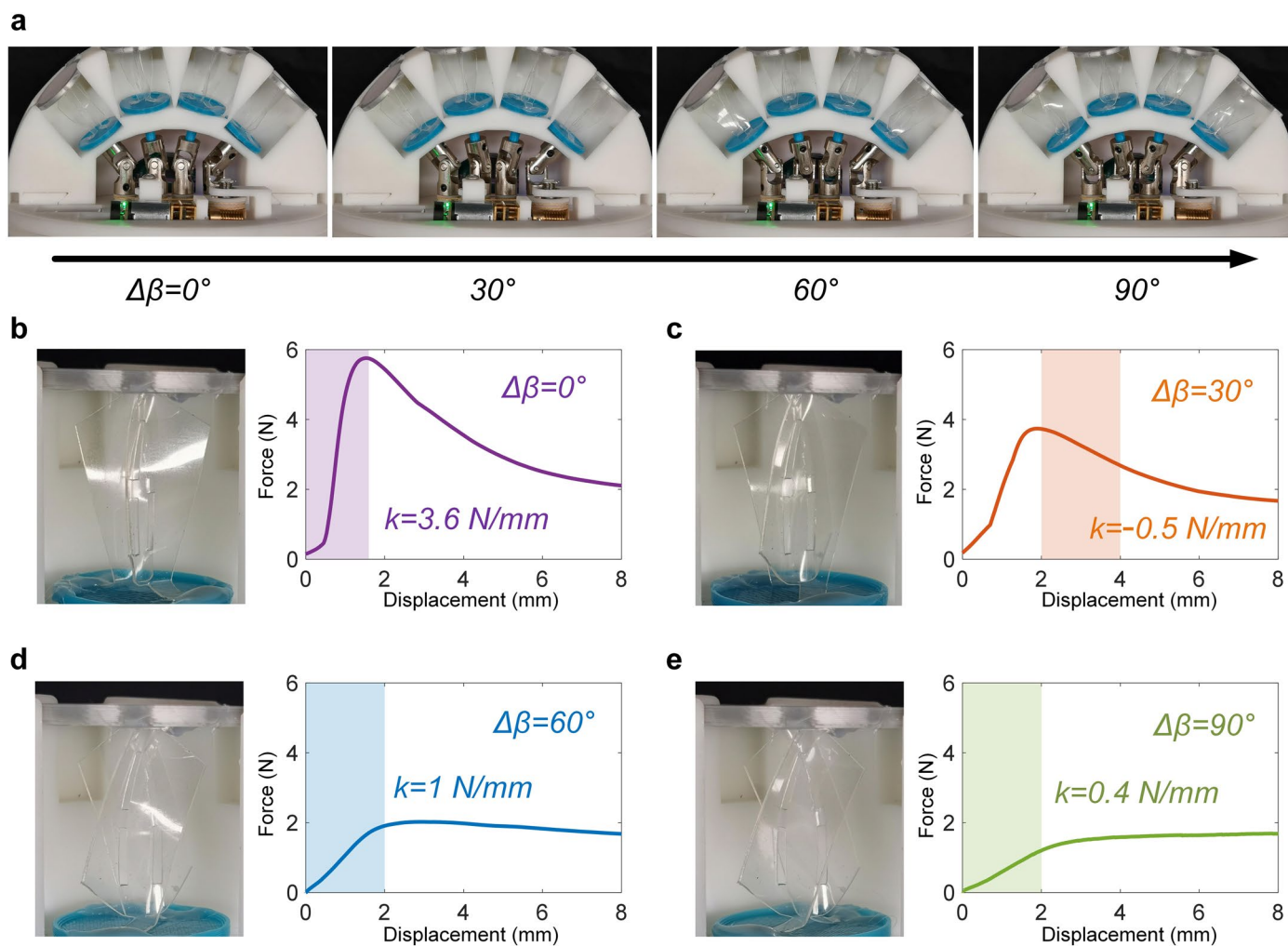
loosely packed structure, while inward bending shows densely packed structure, as compared with the initial state, indicating resistance increase for outward bending and decrease for inward bending.



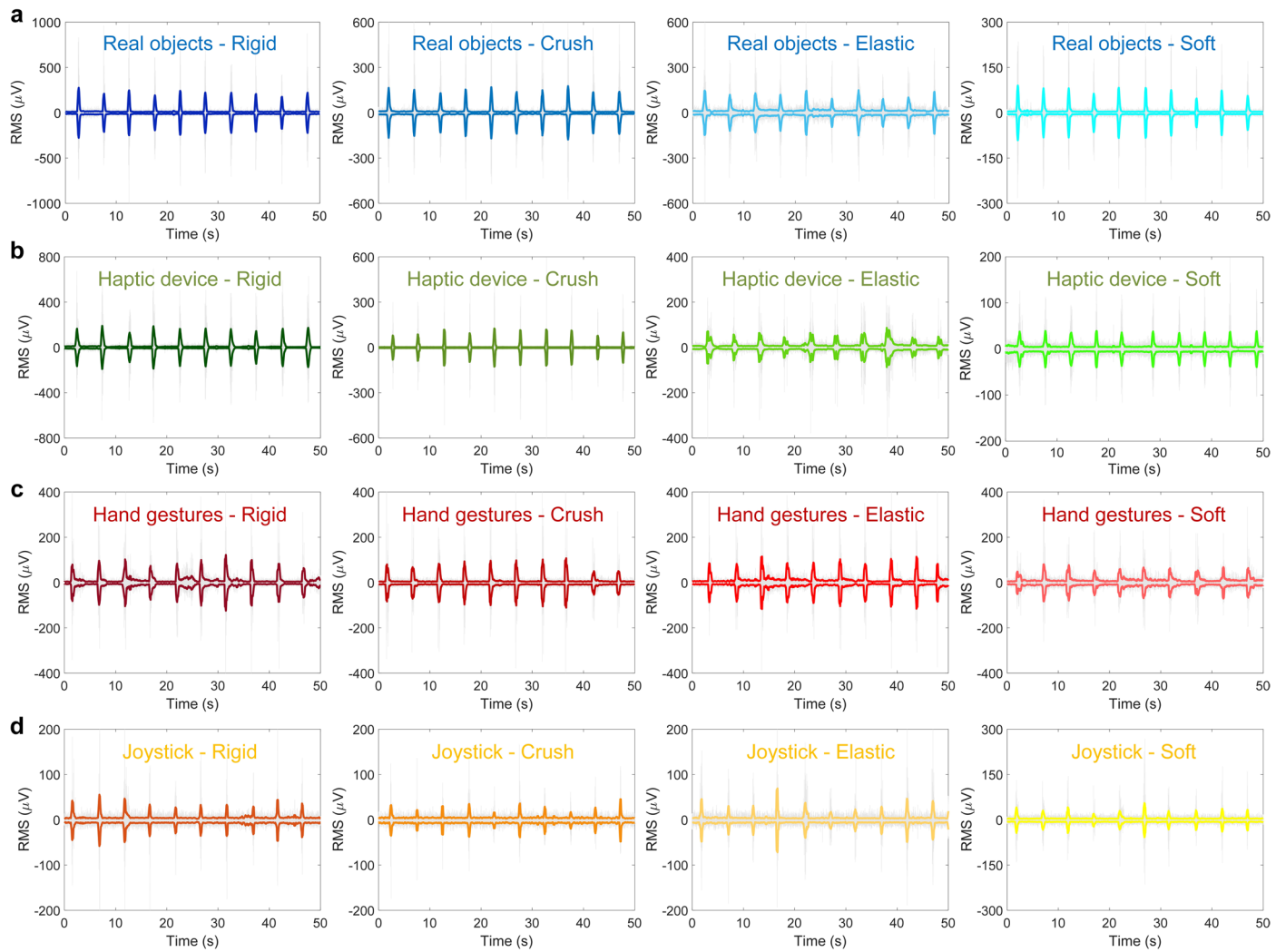
Extended Data Fig. 4 | Mechanical structure of the in-hand haptic device.

a, Exploded-view schematic illustration of the spherical in-hand device with five synchronously controlled origami buttons. The slide guide is utilized to confine the compression range (10 mm) of the origami button. The universal joints are used for transmitting the rotations about the vertical axis between the top and bottom plates of curved origami modules. **b**, Schematic of the actuation system.

The cable is actuated by an on-board micromotor through worm gears. A tension roller is used for the pre-tension of the cable, to avoid the slide between the cable and the rollers. **c**, Synchronous actuation of the origami buttons. A SI-MO (single input–multiple output) actuation strategy is constructed based on cable routing. The red arrow denotes the driving roller, and the blue ones denote follow-up rollers.

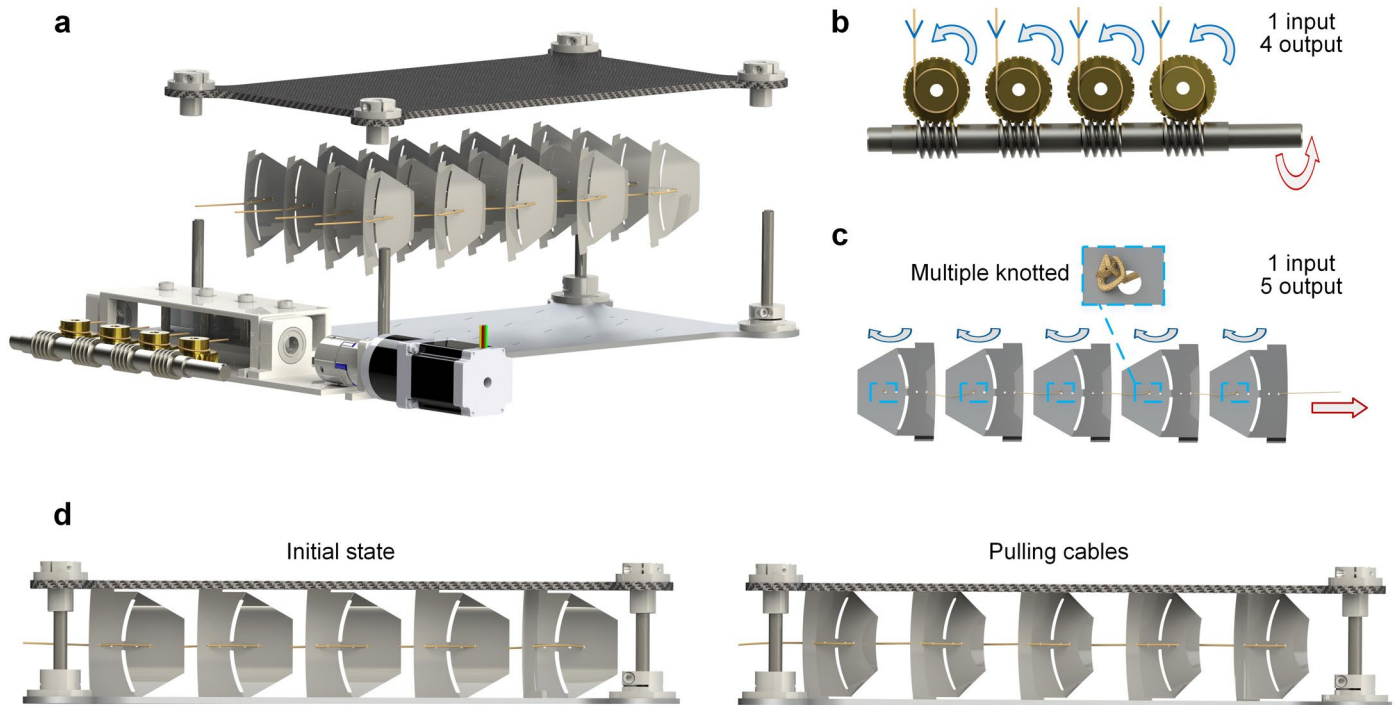


Extended Data Fig. 5 | Stiffness manipulation of the in-hand device. **a**, Synchronous control of the folding angles of the curved origami buttons. **b–e**, Optical images and the corresponding force–displacement relationships of a curved origami button with folding angle $\beta = 120^\circ$ under different control angles $\Delta\beta = 0^\circ$, 30° , 60° , and 90° .



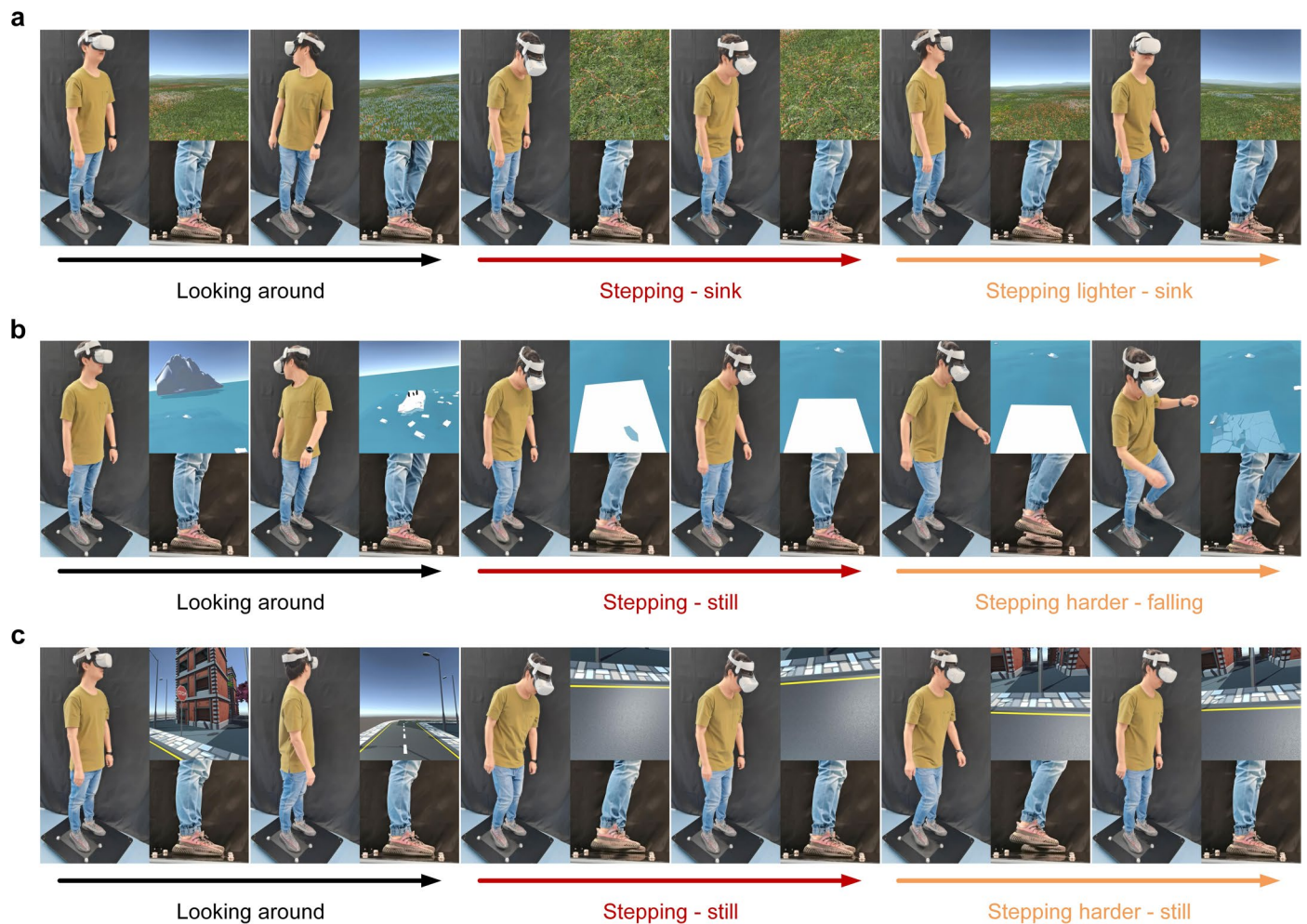
Extended Data Fig. 6 | Recorded EMG of the upper limb. a-d, Raw EMG data with a sampling frequency of 2,000 Hz and the corresponding RMS value with a sampling interval of 0.25 s. The data were recorded when users tried to grasp four

objects with different stiffness under four different scenarios, including grasping real objects (a), grasping the present haptic device (b), grasping virtual objects through hand gestures (c), and grasping a conventional joystick (d).



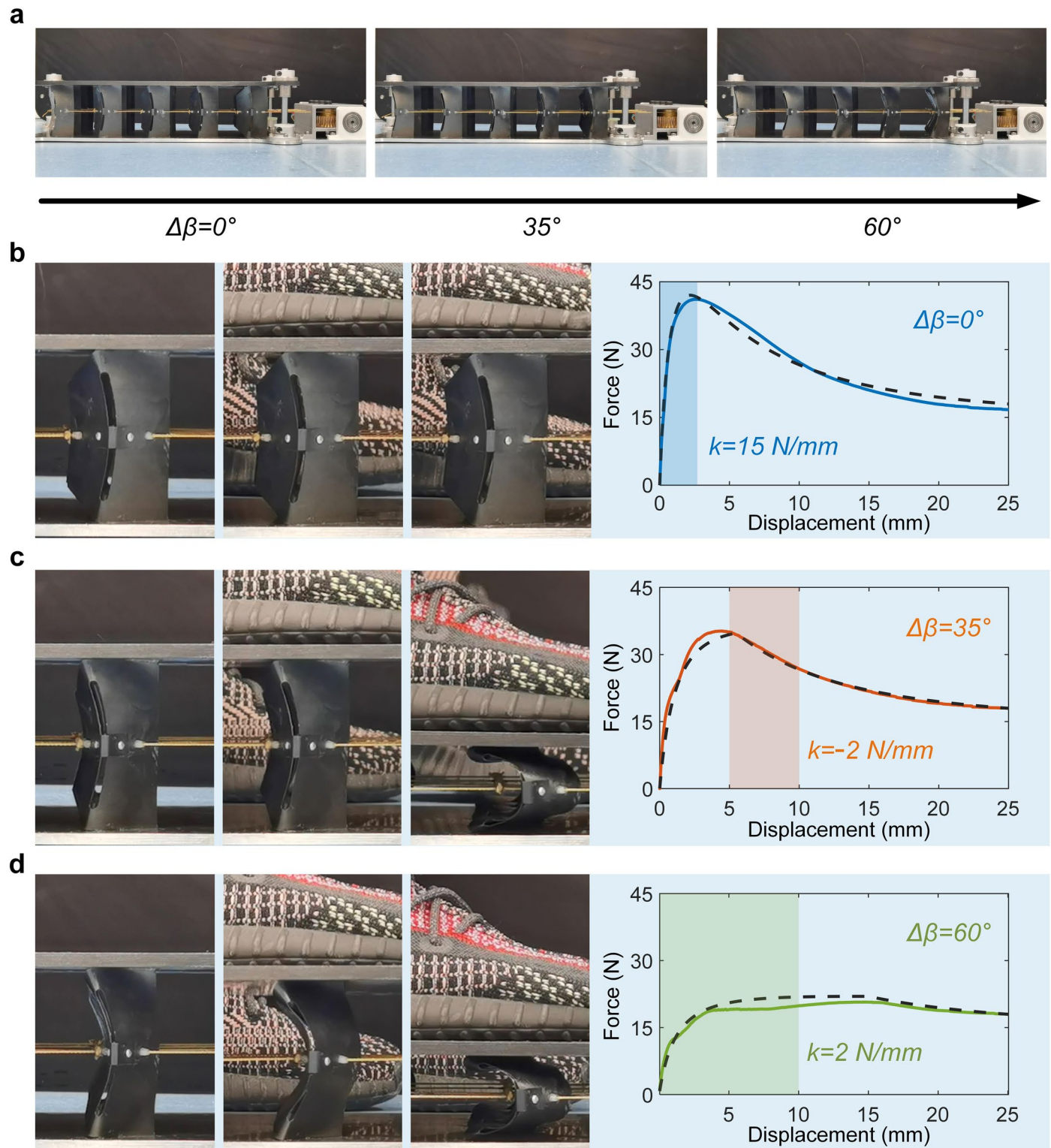
Extended Data Fig. 7 | Mechanical structure of the stepping haptic device. **a**, Exploded-view schematic illustration of the stepping device with synchronously controlled curved origami tessellation. **b**, Schematic of the multihead worm gears transmission. The cable is actuated by a motor through worm gears. Four gears are synchronously controlled by one four-head worm,

making four cables synchronously pulled/released by the motor. **c**, Schematic of the multi-knotted cable-driven transmission. Five knots are evenly made on each cable, rendering the folding of five origami modules synchronously controlled by one cable. The red arrow denotes the input, and the blue ones denote the follow-ups. **d**, Synchronous actuation of the origami tessellation.



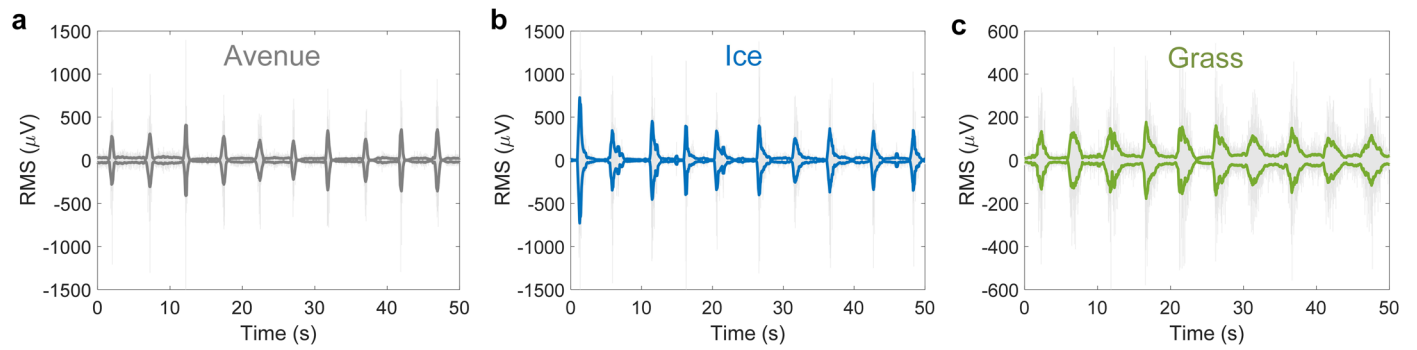
Extended Data Fig. 8 | Snapshots of the immersive whole-body haptic experiences on the stepping device with various virtual scenarios. a, The user experienced low-value positive stiffness in the scenario of grassland, with his feet readily sinking into the virtual ground. **b,** The user experienced negative

stiffness in the scenario of an icy surface, with his whole body keeping still upon a light active stepping while experiencing a real falling upon a hard active stepping. **c,** The user experienced high-value positive stiffness in the scenario of a rigid avenue, with his whole body keeping still upon active stepping.



Extended Data Fig. 9 | Stiffness manipulation of the stepping device.
a, Synchronous control of the folding angles of the curved origami tessellation.
b-d, Optical images of the stepping processes and the corresponding force–displacement relationships of a curved origami module inside the

stepping device with folding angle $\beta = 120^\circ$ under different control angles $\Delta\beta = 0^\circ, 35^\circ,$ and 60° . Solid lines are measured results and dash lines denote theoretical ones.



Extended Data Fig. 10 | Recorded EMG of the lower limb. a-c, Raw EMG data with a sampling frequency of 2,000 Hz and the corresponding RMS value with a sampling interval of 0.25 s. The data were recorded when users stepped on

the stepping device with three different stiffness, including high-value positive stiffness simulating a rigid avenue (a), negative stiffness simulating an icy surface (b), and low-value positive stiffness simulating a soft grassland (c).

Reporting Summary

Nature Portfolio wishes to improve the reproducibility of the work that we publish. This form provides structure for consistency and transparency in reporting. For further information on Nature Portfolio policies, see our [Editorial Policies](#) and the [Editorial Policy Checklist](#).

Statistics

For all statistical analyses, confirm that the following items are present in the figure legend, table legend, main text, or Methods section.

n/a Confirmed

- The exact sample size (n) for each experimental group/condition, given as a discrete number and unit of measurement
- A statement on whether measurements were taken from distinct samples or whether the same sample was measured repeatedly
- The statistical test(s) used AND whether they are one- or two-sided
Only common tests should be described solely by name; describe more complex techniques in the Methods section.
- A description of all covariates tested
- A description of any assumptions or corrections, such as tests of normality and adjustment for multiple comparisons
- A full description of the statistical parameters including central tendency (e.g. means) or other basic estimates (e.g. regression coefficient) AND variation (e.g. standard deviation) or associated estimates of uncertainty (e.g. confidence intervals)
- For null hypothesis testing, the test statistic (e.g. F , t , r) with confidence intervals, effect sizes, degrees of freedom and P value noted
Give P values as exact values whenever suitable.
- For Bayesian analysis, information on the choice of priors and Markov chain Monte Carlo settings
- For hierarchical and complex designs, identification of the appropriate level for tests and full reporting of outcomes
- Estimates of effect sizes (e.g. Cohen's d , Pearson's r), indicating how they were calculated

Our web collection on [statistics for biologists](#) contains articles on many of the points above.

Software and code

Policy information about [availability of computer code](#)

Data collection

The force-displacement relationships, as well as the cyclic tests of the curved origami, are measured through uniaxial compression tests with a universal testing machine (UTM1202, Suns Inc.). The resistance of the AgNWs-coated curved origami and the real-time current of the system during the stiffness tuning process are collected by a data acquisition system (DMM6500, Keithley Inc.). A wireless EMG sensor (PicoEMG, Cometa Systems Inc.) was utilized to record the action voltages during active haptics. An ECG sensor (PC-80B, Heal Force Inc.) was utilized to record the heart rate during active stepping. VR environments are designed with Unity (Unity Technologies Inc.), and are wirelessly projected into the VR device (Oculus Quest2, Meta Inc.). The data collected during the experiment with the volunteers can be downloaded from <https://github.com/EMLQ/AMH>. The data is available via Zenodo at <https://doi.org/10.5281/zenodo.7789004>.

Data analysis

The data plots were processed by OriginLab 2021 or by customized programs in MATLAB 2021.

For manuscripts utilizing custom algorithms or software that are central to the research but not yet described in published literature, software must be made available to editors and reviewers. We strongly encourage code deposition in a community repository (e.g. GitHub). See the Nature Portfolio [guidelines for submitting code & software](#) for further information.

Data

Policy information about [availability of data](#)

All manuscripts must include a [data availability statement](#). This statement should provide the following information, where applicable:

- Accession codes, unique identifiers, or web links for publicly available datasets
- A description of any restrictions on data availability
- For clinical datasets or third party data, please ensure that the statement adheres to our [policy](#)

All data needed to evaluate the conclusions in the papers are present in the paper and/or the Supplementary Information. The data collected during the experiment with the volunteers can be downloaded from <https://github.com/EMLQ/AMH>.

Human research participants

Policy information about [studies involving human research participants and Sex and Gender in Research](#).

Reporting on sex and gender	Twelve participants (nine males and three females) took part in these experiments.
Population characteristics	Twelve healthy 22 to 35-year-old participants without any disability, hand injury or nerve disease took part in these experiments.
Recruitment	Participation was fully voluntary and was recruited from Westlake University. All subjects provided informed consent before the tests and have no self-selection bias that are likely to impact results.
Ethics oversight	All experiments on human were approved by the Ethics Committee of Westlake University (No. 20220621JHQ001, and No. 20220721JHQ001).

Note that full information on the approval of the study protocol must also be provided in the manuscript.

Field-specific reporting

Please select the one below that is the best fit for your research. If you are not sure, read the appropriate sections before making your selection.

Life sciences Behavioural & social sciences Ecological, evolutionary & environmental sciences

For a reference copy of the document with all sections, see [nature.com/documents/nr-reporting-summary-flat.pdf](https://www.nature.com/documents/nr-reporting-summary-flat.pdf)

Life sciences study design

All studies must disclose on these points even when the disclosure is negative.

Sample size	Sample sizes were chosen according to relevant reports in the literature. Most haptics-related human studies involved 1~12 subjects. Here, 12 samples (9 males and 3 females) were used in our study to validate the stiffness perception.
Data exclusions	No data were excluded from the analyses.
Replication	At least 3 trials for each test were taken and used in the data analysis; all attempts at replication were successful.
Randomization	The relative tests covered all participants, both male and female. Randomization was not relevant to the study, because the main purpose of this study is to test the performance of the proposed haptic devices rather than studying the sensitivities of stiffness perceptions.
Blinding	The investigator was not blinded to group allocation during the experiment. Blinding was not relevant because the main purpose of the study was to validate the performance of the proposed haptic devices. Analyses were conducted using identical quantitative, pre-established analysis procedures regardless of which group it is.

Reporting for specific materials, systems and methods

We require information from authors about some types of materials, experimental systems and methods used in many studies. Here, indicate whether each material, system or method listed is relevant to your study. If you are not sure if a list item applies to your research, read the appropriate section before selecting a response.

Materials & experimental systems

n/a	Included in the study
<input checked="" type="checkbox"/>	<input type="checkbox"/> Antibodies
<input checked="" type="checkbox"/>	<input type="checkbox"/> Eukaryotic cell lines
<input checked="" type="checkbox"/>	<input type="checkbox"/> Palaeontology and archaeology
<input checked="" type="checkbox"/>	<input type="checkbox"/> Animals and other organisms
<input checked="" type="checkbox"/>	<input type="checkbox"/> Clinical data
<input checked="" type="checkbox"/>	<input type="checkbox"/> Dual use research of concern

Methods

n/a	Included in the study
<input checked="" type="checkbox"/>	<input type="checkbox"/> ChIP-seq
<input checked="" type="checkbox"/>	<input type="checkbox"/> Flow cytometry
<input checked="" type="checkbox"/>	<input type="checkbox"/> MRI-based neuroimaging